Using nanoindentation to quantify the mechanical profile of Wufeng-Longmaxi Formation in Southwest China: Link to sedimentary conditions

Jianfeng Wang [a, c*], Chao Yang [b**], Yuke Liu [d], Wenmin Jiang [a], Yun Li [a], Ting Zhang [e, f], Yijun Zheng [a], Yuhong Liao [a], Qiuli Huo [g, h, i], Li Fu [g, h, i], Yusheng Wang [g, h, i], Ping'an Peng [a], Yongqiang Xiong [a]

a. State Key Laboratory of Deep Earth Processes and Resources, Guangzhou Institute of Geochemistry, Chinese Academy of Sciences, Guangzhou 510640, *PR* China

b. Guangzhou Institute of Energy Conversion, Chinese Academy of Sciences, Guangzhou 510640, *PR* China

c. The Njord Centre, Departments of Geosciences and Physics, University of Oslo, Blindern, 0316 Oslo, Norway

d. Research Institute of Petroleum Exploration and Development, Beijing 100083, *PR* China

e. Key Laboratory of Petroleum Resources Research, Gansu Province, Lanzhou 730000, *PR* China

f. Research Center for Oil and Gas Resources, Northwest Institute of Eco-Environment and Resources, Chinese Academy of Sciences, Lanzhou 730000, *PR* China

g. Exploration and Development Research Institutle of PetroChina Daqing Oilfield Co., Ltd., Daqing 163712, *PR* China

h. State Key Laboratory of Continental Shale Oil, Daqing, 163712, *PR* China

i. Heilongjiang Provincial Key laboratory of Continental Shale Oil, Daqing, 163712, *PR* China

* Corresponding Authors: Jianfeng Wang; wangjianfeng@gig.ac.cn;

Chao Yang; yangchao@ms.giec.ac.cn

删除[JianFeng Wang]: **f**

删除[JianFeng Wang]: **shale**

删除[JianFeng Wang]:

设置格式[JianFeng Wang]: 正文, 缩进: 首行缩进: 11 字符, 行距: 2 倍行距

Abstract

The fine construction of a continuous mechanical profile for the Wufeng to Longmaxi (WF-LMX) Formation sequence is crucial for designing hydraulic fracturing projects in shale gas development. However, the microscale mechanical profile of WF-LMX Formation shale and its relationship to sedimentary conditions are poorly understood. This study investigates the mechanical profile of the WF-LMX Formation sequence using nanoindentation. A total of 27 cutting samples were collected at one to one-half meter intervals from the Sanquan-1 well. Nanoindentation testing, rock mineralogy, major element analysis, and porosimetry were performed. The results showed that the WF-LMX shales in this study region were deposited in a passive continental margin environment, primarily from biogenic silica. Mechanical properties (hardness, fracture toughness, Young's modulus, and brittle index) varied synchronously with mineral and organic content across the vertical drilling profile, reflecting changes in lithology and sedimentary facies within the WF-LMX Formation. Shales in the upper part of the WF Formation and lower part of the LMX Formation, belonging to the deep-water shelf facies, exhibited high mechanical properties. Quartz and clay play a dominant role in controlling shale mechanics, while the minor rock constituents, nanoporosity have little effect. In particular, biogenic silica (authigenic quartz) plays an important role in increasing the brittleness of shale. The effect of shale constituents on micromechanics is essentially controlled by the sedimentary environment. Additionally, the potential of using nanoindentation to effectively assess shale brittleness was also demonstrated. This study provides a continuous and accurate interpretation profile of mechanical parameters and is helpful in determining favorable intervals for hydraulic fracturing in the design of shale gas development.

删除[JianFeng Wang]: f

删除[JianFeng Wang]: , in a warm and humid climate in a predominantly freshwater environment

删除[JianFeng Wang]: s

Keywords: Wufeng-Longmaxi Formation shale, sedimentary environment, mechanical profile, mineralogy, nanoindentation

删除[JianFeng Wang]: f

1 Introduction

Shale gas is a significant unconventional hydrocarbon resource in China, and occurs in shale-dominated formations with low porosity and low permeability (Zou et al., 2010). Realizing commercial development of shale gas requires large-scale reservoir fracturing of shale formations (Guo et al., 2014). The optimal design of reservoir stimulation (i.e., hydraulic fracturing) highly depends on the reliable measurement of the mechanics of shale at different scales, which remains an ongoing challenge (Rickman et al., 2008, Sone and Zoback 2013a, b). In the past, the uniaxial/triaxial compression and the acoustic emission tests were the most common methods to investigate the mechanical properties of shale rock. These tests are conducted on centimeter-sized cores, thus obtaining shale mechanics at core scale. Although these macroscopic mechanical testing methods can provide reliable and directly applicable rock mechanics data for exploration and development, they are always flawed, especially when mechanical characterization of the entire shale formation is required to optimize favorable fracture intervals, since they rely on bulky core samples that are typically difficult to obtain (Alramahi and Sundberg 2012, Sone and Zoback 2013a).

Nanoindentation, a technique widely used in micromechanical characterization, is increasingly being used to evaluate the micromechanical properties of shales (Ulm et al., 2005). It involves pressing a hard needle tip to press into the surface of the material, thus requiring small sample volumes on the millimeter scale. Because drill cuttings (at the millimeter scale) can meet

66 the requirements of nanoindentation mechanical testing and are readily available, the
67 nanoindentation can achieve accurate mechanical characterization of the entire shale formation.
68 By adjusting the indentation depth or applied load, elastic-plastic parameters such as hardness and
69 Young's modulus of materials can be quickly derived from the load-displacement curves (Oliver
70 and Pharr 1992). In addition, by developing mathematical models, scholars have also used
71 indentation data to calculate other mechanical parameters, including fracture toughness
72 characterizing the ability of a material to resist crack propagation, and brittleness index
73 quantifying the fracturability of materials (Lawn and Marshall 1979, Ma et al. 2023). In order to
74 determine the micromechanical properties of shales by nanoindentation, it is crucial to develop an
75 appropriate indentation protocol, highlighting the importance of establishing a well-designed
76 approach in this field, because shales have a more pronounced size effect and transverse
77 heterogeneity at the microscale (Ulm and Abousleiman 2006, Wang et al., 2022a, 2023, Yang et al.,
78 2020). Currently, a statistical grid nanoindentation scheme is widely used, which is based on
79 averaging a large amount of mechanical data from a series of indentations performed over a
80 sufficiently large area and using large indentation loads (200-500 mN) (Abedi et al., 2016, Gupta
81 et al., 2018, 2020, Kumar et al., 2012, Long et al., 2021, Shi et al., 2019a, 2019b, 2020, Shukla et
82 al., 2013, Zhao et al., 2019). The use of a relatively large load is to indent a large volume to
83 involve more matrix phases in each indentation (i.e., to reduce the impact of size effects), and the
84 use of a nanoindentation campaign is to make the results more statistically significant (i.e., to
85 reduce the impact of heterogeneity). A large number of indentation cases indicate that this method
86 is reliable and scientific for obtaining the micromechanical properties of shale. Besides, some
87 research indicates that the Young's modulus determined by acoustic emission testing correlates

well with measurements obtained by nanoindentation. (Kumar et al., 2012). In general, the mechanical properties (mainly Young's modulus) measured by nanoindentation can provides us with an efficient approach to analyze the mechanical properties and variation patterns of specific shale formation at the microscopic scale.

The Wufeng-Longmaxi (WF-LMX) Formation shales are the primary marine formations for shale gas exploration and development in southern China, with commercial developments successfully implemented in several locations including Fuling, Changning, and Weiyuan in Sichuan Province, China (Zou et al., 2010). In particular, the marine black shales of the WF-LMX Formation were predominantly deposited in a deep-water shelf environment characterized by strong reducing conditions (Zou et al., 2010). To date, extensive research has been conducted and documented on the geologic characteristics of areas conducive to WF-LMX shale gas accumulation (Guo and Zeng 2015, Yan et al., 2018, Zheng et al., 2022, Zou et al., 2010). Currently, engineering challenges have emerged as critical to the success of shale gas development. Among these, rock mechanics research, particularly as it relates to hydraulic fracturing, has been at the forefront of research efforts. Previous mechanical research on the WF-LMX shale was mainly based on macromechanical testing (Guo et al., 2019, Jia et al., 2021b). Although many significant achievements and insights have been made to guide exploration and production, several challenges remain, such as determining exactly how changes in stratigraphy correlate with changes in the mechanical properties of a shale sequence, which can then be used to identify the most suitable intervals for hydraulic fracturing operations (Sethi et al., 2024). Previous studies have attempted to use macroscopic testing to establish the relationship between macroscopic mechanics and sedimentary conditions (Li et al., 2024, Sethi et al., 2024), while they are not able

to characterize shale strata continuously and their inability to accurately depict the correlation between shale mechanics and sedimentary condition, especially for the fragile shale samples. Nanoindentation can overcome sampling problems, and a single mechanical test can simultaneously obtain these mechanical parameters. Recent literature mainly discusses the selection of indentation method (Du et al., 2021, Jia et al., 2021a, Shi et al., 2019b, Wang et al., 2022b), fluid influence (Yang et al., 2018, Yang et al., 2016), and component analysis of small sample size for the study of WF-LMX shale mechanics (Long et al., 2021). Few studies concerning the geological effects has been done for the micromechanical properties of shales (Charlton et al., 2023). To the best of our knowledge, there have been no investigations focusing on the microscale mechanical properties, namely elasticity, plasticity, toughness, and brittleness, of the marine shale of the WF-LMX Formation along the southeastern margin of the Sichuan Basin and how these properties are related to sedimentary conditions.

删除[JianFeng Wang]: f

In this study, we aim to use nanoindentation technology to perform a thorough mechanical characterization of WF-LMX shales at the microscale and to quantitatively assess the mechanical profile of WF-LMX shales. Specifically, in order to obtain micromechanical parameters, we particularly used a novel method to calculate the shale brittleness index based on nanoindentation data. Additionally, we aim to correlate the measured micromechanical data with the sedimentary conditions (e.g., redox condition and bedding) and rock physics (petromineralogy, reservoir space) of the WF-LMX Formation. This correlation will enable us to identify the controlling factors of shale mechanics at the micro-scale and to investigate how lithofacies influence the micromechanical profile of WF-LMX shales. In general, this mechanical study of WF-LMX shales in the whole layer using nanoindentation technique overcomes the limitations of traditional

删除[JianFeng Wang]: formation

删除[JianFeng Wang]: s

mechanical testing associated with sample availability. This approach provides a continuous and accurate interpretation profile of mechanical parameters for the design of shale gas development.

2 Geological setting and sampling shale samples

The Sichuan Basin and surrounding regions were characterized as stagnant basins during the Late Ordovician to Early Silurian, resulting in the formation of extensive low-energy and anoxic sedimentary environments (Chen et al., 2014). During this period, two significant global transgressions occurred, which contributed to extensive organic-rich shale intervals within the WF Formation and the bottom part of the LMX Formation (see Figure 1a). The black shale gradually shifted from the central sedimentary region to the source region (as shown in Figure 1a), while the paleoenvironment gradually evolved from deep-water shelf environments to semi-deep-water environments and finally to shallow-water shelf environments (Guo and Zeng 2015).

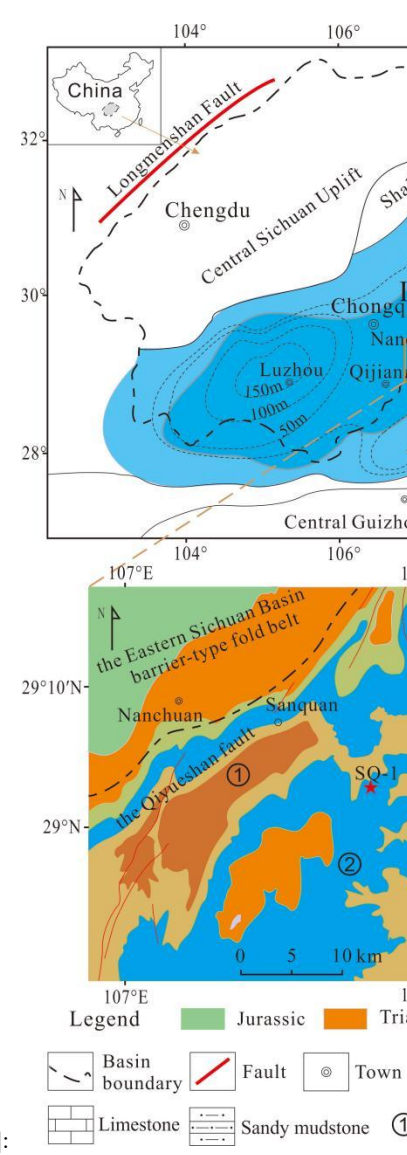

删除[JianFeng Wang]:

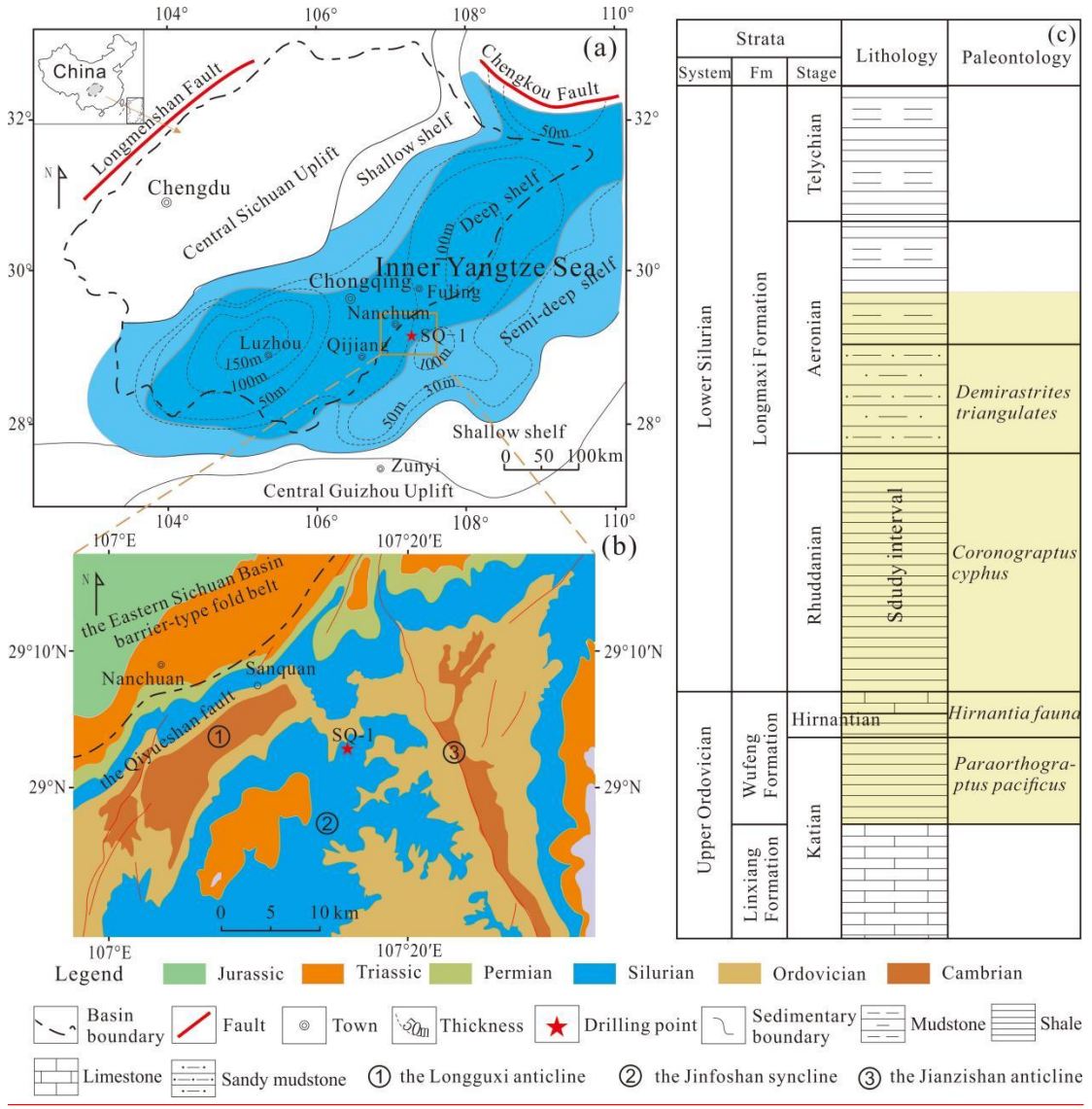

Figure 1. (a) shows a paleogeographic map of the Sichuan Basin and adjacent regions during the Early Silurian. (b) shows the regional, structural and geological profiles of the Sanquan region, highlighting the exposed strata and the Sanquan-1 well. (c) shows the stratigraphic, lithologic, and paleontologic column, along with the intervals under study (modified from (Zheng et al., 2018)). Fm = Formation.

The Sanquan-1 (SQ-1) well, located in Sanquan Town, Nanchuan District, Chongqing City, within the Sichuan Basin of China (as shown in Figure 1b), is located on the crest of an anticline

and to the east of the Qiyue Shan Fault (see Figure 1b). Core shale samples were collected from the Upper Ordovician Wufeng Formation and the lower part of the Silurian Longmaxi Formation (as shown in Figure 1c). The stratigraphy of the SQ-1 well consists of muddy limestone, siliceous shale, carbonaceous shale, black shale, sandy mudstone and mudstone in sequence from base to top. According to biostratigraphy, petrography and gamma-ray (GR), sequence stratigraphy of Well SQ-1 can be distinguished (Figure 1c). There are two sections in the Longmaxi Formation of the SQ-1 well: the Rhuddanian and Aeronian stages. The Rhuddanian Stage, ranging from 60.5 to 84.7 meters in depth, consists of black carbonaceous and black shale. The Aeronian Stage, from 11 to 60.5 meters, consists of black shale and grayish-black argillaceous sandstone (Figure 1c). The WF Formation (84.7-90.0 m) contains two parts, the Katian Stage (86.0-90.0 m) and the Hernantian Stage (84.7-86.0 m) (Zheng et al., 2018).

3 Samples and method

3.1. Shale rock samples

Shale core samples were systematically collected from the WF-LMX Formation within the wellbore at intervals of one to one and one-half meters from the bottom up. A total of 27 core samples were collected for analysis. These samples have been used in previous geological and petrological studies targeting for shale gas exploration in WF-LMX shales (Yang et al., 2020, Zheng et al., 2018, 2022). Most of the information regarding total organic carbon (TOC) assessment, mineral composition analysis, major element analysis, experimental assessment of total porosity by mercury injection capillary pressure (MICP), and characterization of nanopore structures by N_2/CO_2 gas adsorption techniques is provided in our previous research (Zheng et al.,

删除[JianFeng Wang]: formation

2018), and the related data can be found in Tables S1-S2. It is noted that previous studies of these samples have focused primarily on the organic geochemical properties, mineralogy, and porosity of the WF-LMX shale Formation. In contrast, our research primarily investigates the coupling relationship between the micromechanical properties and the sedimentary environment of these shales.

删除[JianFeng Wang]: formation

删除[JianFeng Wang]: s

3.2 Sample preparation

Shale samples were prepared with cuttings for nanoindentation test, generally 1-10 mm thick (Figure 2a). We chose shale samples oriented perpendicular to the bedding plane (designated X1) and those oriented parallel to the bedding plane (designated X3) (Figure 2b), first cut them into ~5 mm thick chips, then impregnated them and cemented them with resin, and ground and polished it using silicon carbide abrasive papers of various mesh sizes ranging from 50 to 2000 grit. This was followed by the application of diamond suspension fluid with particle diameters of 9, 3, and 1 micrometer for detailed polishing (Yang et al., 2020). Finally, an IM4000 argon ion mill was used for an additional 1-2 hours of polishing to achieve a very smooth surface. The average roughness (measured as root mean square roughness, Rq) of the shale surface, which measures $30 \times 30\ \mu m^2$ and was measured using atomic force microscopy, is less than 100 nm (Wang et al., 2022b). Figure 2c shows a typical optical microscopy image of the shale sample after grid nanoindentation.

3.3 Optical microscopy

The mineralogy was examined using an Olympus 4500P optical microscope under reflected light, which was integrated with the nanoindentation system. This high-resolution optical microscope offers magnifications ranging from 200× to 4000×, making it suitable for precise visualization of the surface area prior to nanoindentation testing.

3.4 Scanning Electron Microscope (SEM)-Energy Dispersive Spectroscopy (EDS) imaging

Following the nanoindentation tests, we used a Hitachi S8010 Scanning Electron Microscope (SEM) integrated with Energy Dispersive Spectroscopy (EDS) to examine the indentations formed on the shale surface. Deviating from standard pre-treatment procedures, the specimens were not coated with a gold layer prior to testing to avoid potential damage to the indentation sites and to ensure unobstructed observation of the indentations. The phase distribution diagram based on elemental composition was quantified by EDS analysis.

3.5 Nanoindentation tests

3.5.1 Nanoindentation and theoretical background

Mechanical nanoindentation tests were performed using an Anton Paar TTX NHT^3 nanoindenter with a diamond Berkovich indenter tip with a radius of curvature between 50 and 100 nm (shown in Figure 2a). A high-resolution optical microscope was integrated into the indenter for precision. Loads ranging from 0.1 to 500 mN were applied to the indenter as it contacted and penetrated the sample surface.

Before performing the indentation tests, a standardized fused silicon sample was used to calibrate the shape of the tip. Thanks to the unique reference ring design of the Anton Paar

instrument, automatic thermal drift correction was implemented to ensure data stability. Figure 2d shows a schematic representation of the indentation profile, while Figure 2e shows a typical load-displacement curve (*P-h* curve) consisting of three distinct phases: loading, holding and unloading. The loading phase includes both elastic and plastic deformation components, while the unloading phase captures only the elastic deformation-related strain recovery (Cheng et al., 2002, Yang et al., 2020). Consequently, the area under the unloading curve is referred to as the elastic energy (U_e), and the area enclosed by both the loading and unloading curves represents the irreversible energy (U_p). The total energy (U_t) is the sum of U_e and U_p (Cheng et al., 2002). By analyzing the *P-h* curve, the hardness (H) and reduced elastic modulus (E_r) of the shale will be derived (Oliver and Pharr 1992, 2004). In this investigation, a Poisson's ratio of 0.3 was assumed for the shale samples to calculate their Young's modulus (E) (Li et al., 2018).

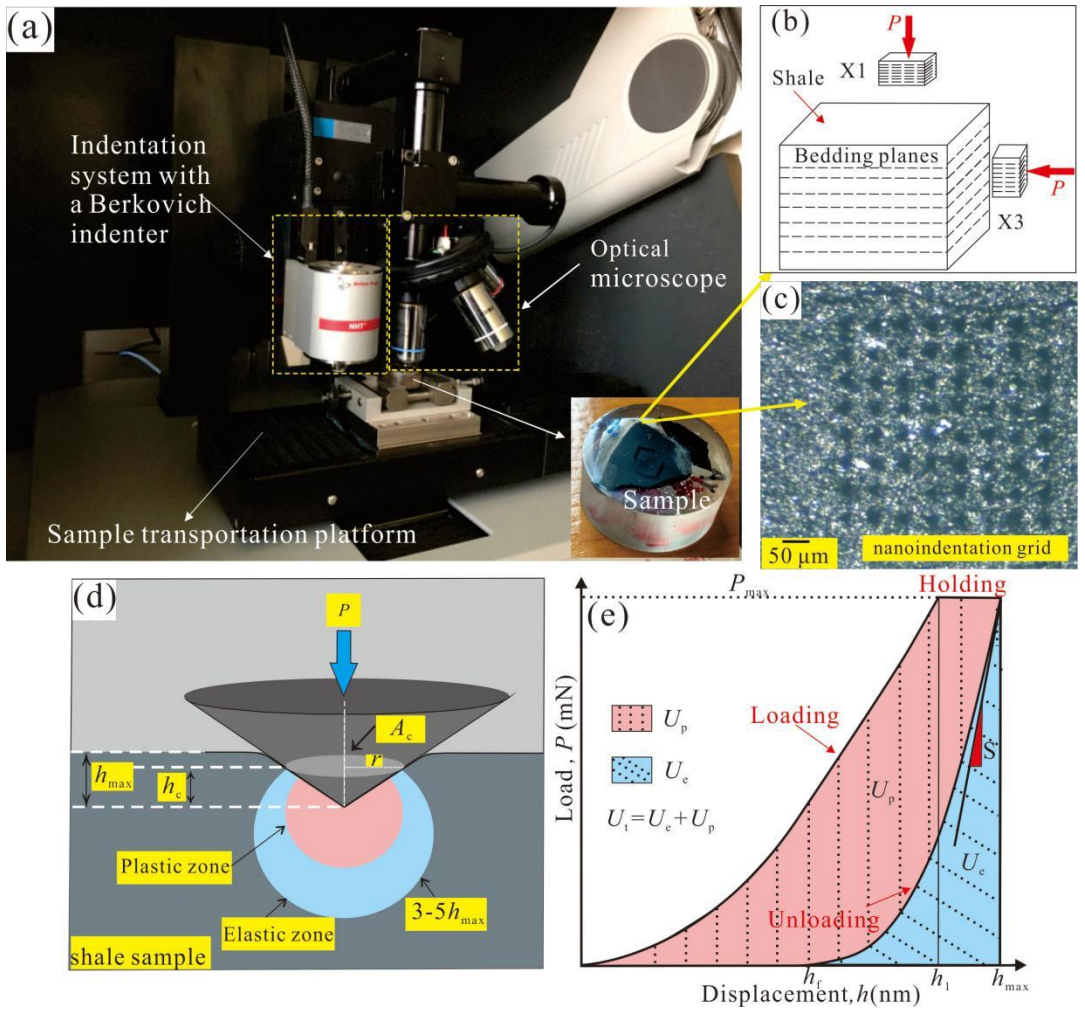

Figure 2. (a) The primary components of the nanoindenter are shown, with the polished specimen in the lower right corner. (b) shows the specimen with X1 and X3 planes, oriented differently for nanoindentation testing. (c) shows typical light microscopy images of a shale sample undergoing nanoindentation. (d) provides a schematic representation of the indentation profile. (e) shows a typical load-displacement (*P*-*h*) curve (modified from (Wang et al., 2023)). Here, *P* is the applied load, P_{max} is the maximum load, *r* is the contact radius, *S* is the contact stiffness, *h* is the indentation displacement, while h_f, h_1, and h_{max} are the residual displacement, the displacement at the onset of the hold phase, and the maximum displacement during nanoindentation, respectively. The elastic-plastic deformation zone under the indenter is 3-5 times h_{max} (Larsson et al., 1996).

3.5.2 Experimental protocols

Constant load holding tests were performed in which the indentation load was applied in a linear fashion until the peak load of 400 mN was reached. Once this peak load was reached, the diamond indenter was held in position for 2 seconds. Finally, the indentation test was completed with a 30-second unloading of the tip. We adopted the statistical nanoindentation method, which is widely used in the mechanical characterization of muti-phase composite materials (Figure 2c). Specifically, the peak load of 400 mN was used (Kumar et al., 2012). Each shale sample surface contained at least 7×7 grid indentations with the distance of at least 60 μm between adjacent indentations (Wang et al., 2022a). Therefore, the size of the indentation areas was approximately 450 × 450 μm^2, which is a much larger representative elementary area (REA) than that proposed by Liu et al. (2018) to ensure an unbiased statistical characterization. Prior to conducting the nanoindentation tests, we first observed the shale surface using a high-resolution optical microscope to determine the representative regions of interest, taking into account the multiscale heterogeneity and mineralogical variability of the shale. We did not find a laminated texture in our shales. The shale surface areas selected for testing exhibited mineralogical characteristics consistent with the overall shale surface.

3.6 Determination of fracture toughness and brittleness index

In this study, the energy-based method was used to calculate the fracture toughness (K_c) of shale (Gautham and Sasmal 2022, Gupta et al., 2020, Liu, 2015, Liu et al., 2016, 2022, Liu 2015, Manjunath and Jha 2019, Zeng et al., 2017, Zeng et al., 2019). After we obtained K_c, the brittleness index (B) based on the mechanical properties can be calculated as (Lawn and Marshall 1979):

$$B = \frac{HE}{K_c} \quad (1)$$

The detailled calculation process can be found in the Test S1 of the Supplementary Material.

3.7 Statistical Analyses

Statistical significance of the correlations between mechanical parameters and mineralogy, TOC content, porosity and pore volume was determined by SPSS 23.0 software with Pearson correlation analyses and two-tailed Student's tests. This statistical analysis provides a range of correlation coefficients and tests designed to assess the magnitude and direction of the relationship between two variables. This allows us to gain a deeper insight into the patterns and relationships in the data, as well as to uncover potential associations that may go beyond the confines of simple linear correlations. All numerical analyses were performed using Origin 2021, Python 2.0 and Microsoft Excel 2016, and all graphs were made by Origin 2021, Corel Draw X8 and Microsoft Excel 2016.

4 Results

4.1 Mineralogy and indentation of shale

4.1.1 Optical properties of shale mineralogy

The core samples are mainly composed of quartz and clays (≥70 vol.%) with small percentages of feldspar, carbonate, pyrite and organic matter. Here, we selected two representative samples (i.e., SQ-80b and SQ-90) in terms of their different mineralogical characteristics (i.e., quartz-rich and clay-rich) to demonstrate the microstructure of the shale. The quartz grains present in the detrital material are translucent and have a grayish white color when viewed under reflected

287 light (Figure 3). They have a variety of irregular shapes characterized by sharp, straight
288 boundaries and are predominantly between 15 and 40 microns in size (Figure 3). It is noteworthy
289 that WF-LMX shales have large amount of authigenic quartz grains, which are usually very small
290 in size, less than 2 μm, and can only be observed by SEM (Milliken et al., 2016, Yang et al., 2020).
291 The clay minerals show dark gray color and are continuously distributed in the shale matrix,
292 constituting the connected skeleton of the shale (Figure 3). Notably, the clays are usually
293 intermixed with nanometer-sized organic matter, forming the organoclay composites (Ma et al.,
294 2015, Yang et al., 2020). Organic matter, consisting mostly of particles smaller than 3 μm, is
295 embedded in matrix voids or intermixed with clay minerals (Figure 3d). Pyrite typically appears as
296 aggregates with dimensions ranging from 1 to 8 μm (Yang et al., 2020). The pyrite and organic
297 matter usually show a grayish white to bright white color under the reflected light. Overall, the
298 quartz-rich shale sample has a coarse-grained texture with large mineral particles such as quartz
299 acting as the supporting skeleton. However, the clay-rich shale has a continuous and fine-grained
300 texture with organoclay composites acting as the framework materials of shale. Notably, the X1
301 plane (as shown in Figures 4a and 4c) exhibits a lower amount of quartz compared to the X3 plane
302 (as shown in Figures 4b and 4d).
303

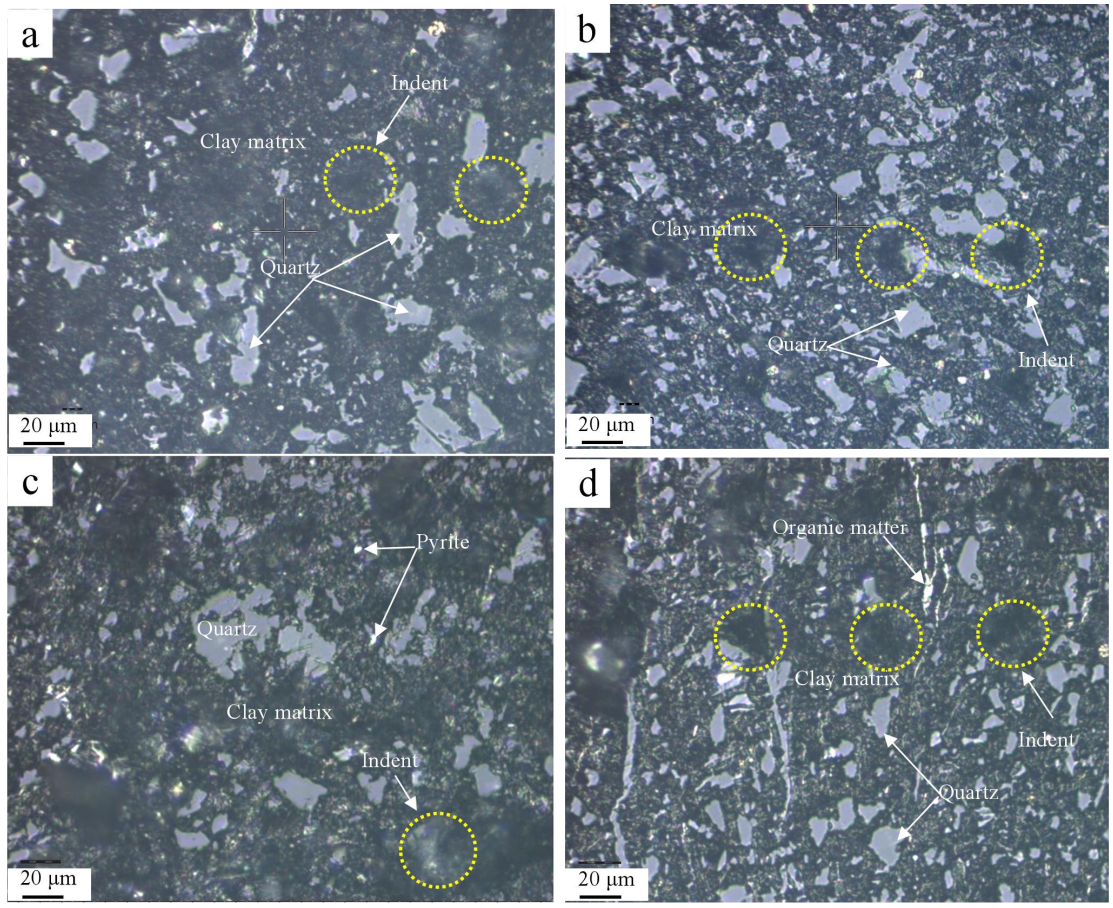

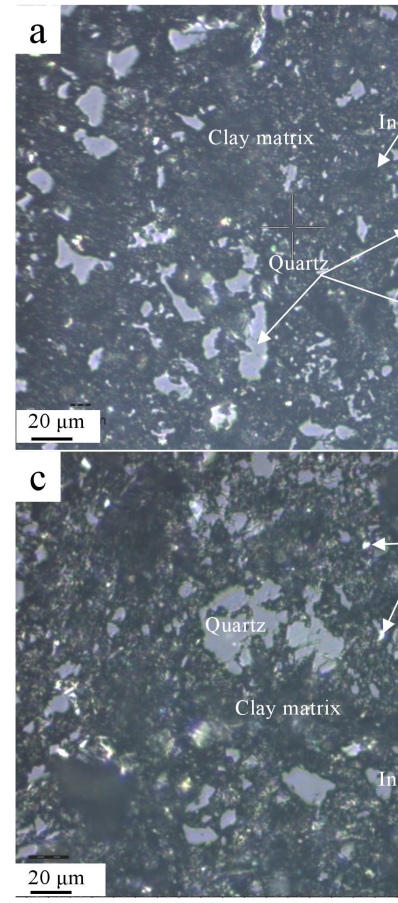

删除[JianFeng Wang]:

Figure 3. Optical microscopy images of the mineralogy of the two representative shale samples. The mineral composition characteristic for (a, b) quartz-rich shale, and (c, d) clay-rich shale. The (a, c) are from X1 plane and (b, d) are from X3 plane. The X1 plane (a, c) of the shale sample has a lower concentration of quartz grains compared to the X3 plane (b, d). The "indent" in (a, b, c and d) represents the indentation residual residual impressions left in the shale.

4.1.2 Nanoindentation of representative microdomains

Figure 4 displays the indents of SQ-78b sample in the X3 plane. Figure 4a shows the panorama of all the indentations. It is observed that some of the indents are located on micro-fractures. Given the strong heterogeneity of the shale, we chose three representative indentation areas for further analysis: the clay-rich area, the organic matter-rich area, and the

316 quartz-rich area. The quartz particle is large, and its surface is very smooth, mainly containing Si
317 and O elements (Figures 4g and 4i). The organic matter in the backscattering diagram appears a
318 black color (Curtis et al., 2012, Zhao et al., 2014), with no fixed form, and is shown in the form of
319 small strips and thin threads (Figure 4f). The clay matrix often combines with the organic matter
320 and mainly contains elements such as Al, Si, C and O (Figures 4e and 4h). The indentation
321 impression in the quartz-rich area measures approximately 20 μm in diameter, while those in the
322 other two areas exceed 30 μm. Microcracks are found around the quartz-rich area, indicating that
323 quartz grain is fractured under the load of 400 mN. In contrast, no significant cracks are observed
324 in the clay-rich and organic matter-rich areas. Furthermore, indentation impressions are clearly
325 visible in the clay-rich and quartz-rich areas. In contrast, no indentation impressions are observed
326 on the surface of the organic matter. This phenomenon has also been found in previous studies
327 (Liu et al., 2019b, Wang et al., 2022c), and is attributed to the high elasticity of organic matter in
328 the high maturity stage.

删除[JianFeng Wang]: a

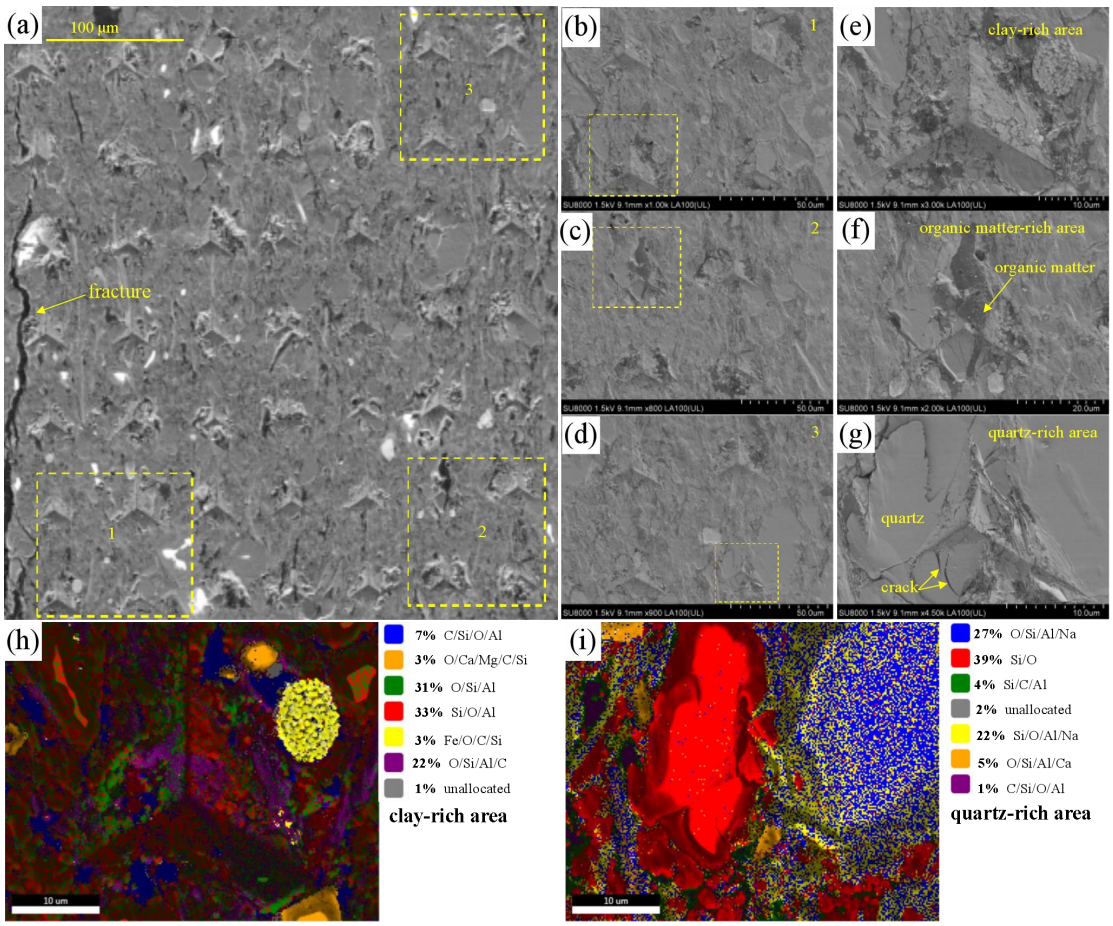

Figure 4. Backscattering (BSE) diagrams (a-g) and phase distribution diagram (h-i) of indent points in different regions. The numbers 1, 2, and 3 in (b-d) represent the corresponding enlarged parts. The phase distributions of (h-i) show the indentations are located on the clay-rich area and quartz-rich area, respectively. The indentation impression in the quartz-rich area has a diameter of about 20 μm, while the diameters of the other two areas are larger than 30 μm. The indent is clearly visible in the clay-rich or quartz-rich area, but not in the organic-rich area.

Figure 5 shows the *P-h* curves of all the indents and three typical indents. Figure 5a shows the maximum displacement ranges from ~3 to 6 μm. The indents present at the fracture zones (as shown in Figure 4) show significant displacements along with pop-in behavior characterized by abrupt jumps in displacement. This phenomenon could possibly be due to the development of

microcracks during the indentation process. We did not use these data for statistical mechanical analysis. The maximum indentation displacement in the quartz-rich area is significantly smaller than those in the organic-rich area (~4900 nm) and clay-rich area (~4900 nm). The E and H of the indentations in the quartz-rich area are the highest, with values of E=31.7 GPa and H=0.93 GPa, respectively, while those in the organic matter-rich area (E=26.7 GPa, H=0.85 GPa) and the clay-rich area (E=26.3 GPa, H=0.77 GPa) are lower (Table 1). Despite the relatively large differences in elasticoplastic parameters, the fracture toughness of these three indents is relatively similar, ranging from 0.79 MPa·$m^{0.5}$ to 0.85 MPa·$m^{0.5}$. The B value for the indent of quartz-rich area is the highest (43.6 μm^{-1}), followed by the indent in the clay-rich area (34.8 μm^{-1}) and the indent in the organic matter-rich area (29.1 μm^{-1}). Overall, the average mechanical parameters obtained are: E=29.4±3.2 GPa, H=0.95±0.41 GPa, K_c=0.90±0.31 MPa·$m^{0.5}$, and B=37.3±10.5 μm^{-1}. Notably, the values of H show a larger variability (43.2% variation) than those of E (10.9 % variation) and K_c (34.4 % variation).

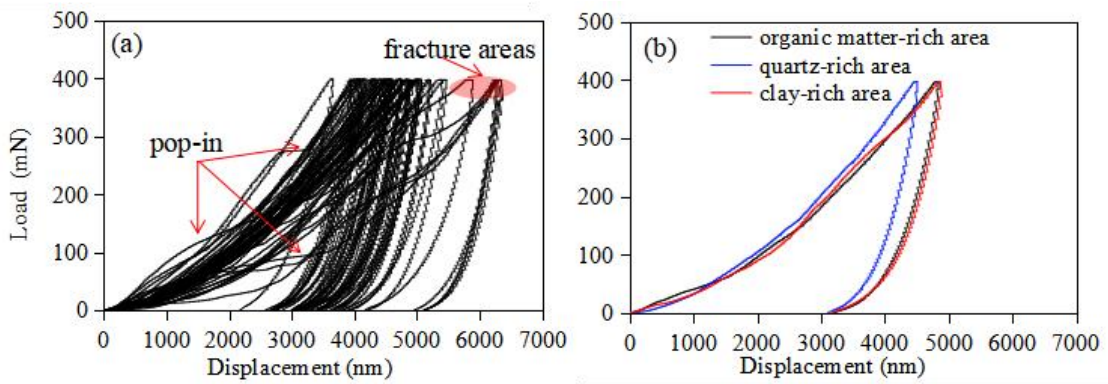

Figure 5. Load-displacement curve of (a) all the nanoindentation points, and (b) three typical indentation points in different areas.

Table 1. Mechanical parameters of nanoindentation points in different regions.

Point	Point of area	E (GPa)	H (GPa)	K_c (MPa·$m^{0.5}$)	B (μm^{-1})
1st	Clay-rich	26.3	0.77	0.79	34.8
13th	Organic matter-rich	26.7	0.85	0.85	29.1
42th	Quartz-rich	31.7	0.93	0.82	43.6
All	All areas	29.4±3.2	0.95±0.41	0.90±0.31	37.3±10.5

360

361 **4.2 TOC, mineralogy, porosity and major elemental characteristics**

362 Using lithofacies analysis and gamma ray (GR) values, previous researchers have divided the
363 WF Formation into two primary sections from base to top: the Transgressive Systems Tract (TST)
364 and the Highstand Systems Tract (HST), while the LMX Formation was divided into TST, HST
365 and LST (lowstand systems tract) from bottom to top for the SQ-1 well (Zheng et al., 2018)
366 (Figure 6). The TOC content of LMX Formation and WF Formation are in the range of 0.53-3.34
367 wt.% (average 1.94 wt.%) and 1.30-6.53 (average 3.74 wt.%), respectively. The quartz content
368 values of LMX Formation and WF Formation are in the range of 19.6-43.6 vol.% (average 29.4
369 vol.%) and 22.7-51.5 vol.% (average 39.3 vol.%), respectively. The clay content values of LMX
370 Formation and WF Formation are in the range of 30.3-54.3 vol.% (average 43.1 vol.%) and
371 28.8-48.1 vol.% (average 35.5 vol. %), respectively. Feldspar content ranges from 10.6 to 20.4
372 vol%, with an average of 16.2 vol%. Conversely, the carbonate and pyrite contents are minimal,
373 typically less than 10 vol% (Table S1). The major oxides in the WF-LMX Formations are SiO_2
374 and Al_2O_3. Other major element concentrations were observed to be <7% (Table S2). The SiO_2
375 content is the highest of all the oxides in the shale samples, ranging from 58.63% to 76.32%. The
376 average SiO_2 content of WF Formation (69.73%) is higher than that of the LMX Formation
377 (61.54%). The average Al_2O_3 contents in LMX and WF Formations are 13.66% and 8.61%,
378 respectively. The excess SiO_2 contents are in the range of 5.93-58.93% (Table S2).

As one moves upward through the drilling profile of the WF-LMX shales, the GR values and TOC content initially increase and then decrease. The quartz content follows a similar pattern to the TOC content, while the clay mineral content shows an opposite trend. Excess silicon is widely distributed in the WF shales (Zheng et al., 2018). Previous research has shown that the excess silicon originates from authigenic silicon in shale, which is closely related to the genesis of siliceous plankton such as diatoms and sponge spicules in sedimentary waters (Schieber et al., 2000). In the SQ-1 well, the excess SiO_2 content varies from low at the bottom, to high in the middle, and then back to low at the top, with the higher values (ranging from 43.04% to 58.93%) being observed in the upper section of the WF Formation. In terms of reservoir space parameters, the total pore volume (V_{total}) and total porosity exhibit ranges of 21.0-41.4 × 10^{-3} cm^3/g and 1.3-6.4%, respectively. The higher values are in the WF Formation, where the average values are 37.6 × 10^{-3} cm^3/g and 4.5%, respectively. In general, both V_{total} and total porosity are positively correlated with the TOC content (Table S1).

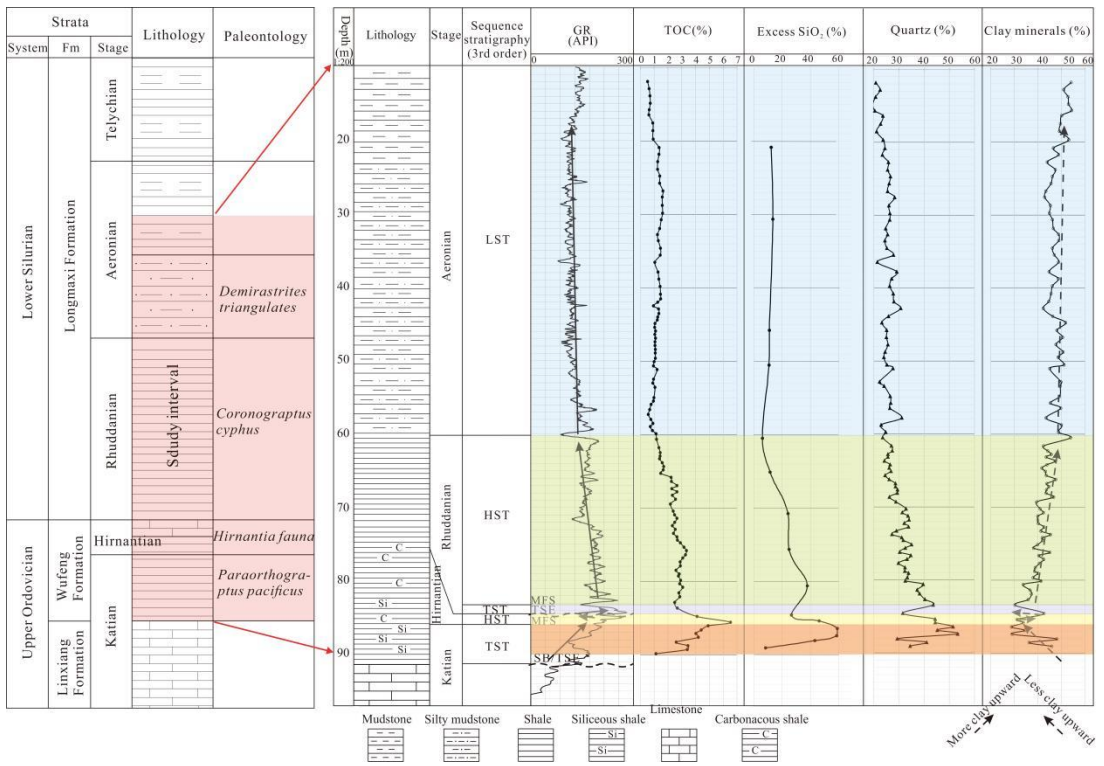

Figure 6. A detailed histogram depicting various properties of the WF-LMX shales, including gamma-ray (GR) intensity, TOC content, excess SiO_2 content, quartz content, and clay content (modified from Zheng et al. (2018)). HST is the highstand systems tract; LST is the lowstand systems tract; TST is the transgressive systems tract.

4.3 Micromechanical profile of WF-LMX shales

Figure 7 shows the longitudinal variations of different micromechanical parameters (E, H, K_c, and B) of WF-LMX Formations in the SQ-1 well. Table S3 presents the corresponding data. Overall, the mechanical parameters in the X1 plane change synchronously with those in the X3 plane. Specifically, they first increase and then decrease from the bottom to the top, which is consistent with the variation of quartz and TOC content in the drilling profile. The highest mechanical property values occur in the Hirnantian and the upper Katian of the WF Formation (85-87.6 m), where the contents of TOC (4.2-6.5 wt.%) and quartz (44.4-53.3%) are also very high (Figure 6, Table S4). In fact, the WF Formation was in a deep-water marine shelf setting during the Hirnantian and the upper Katian stages. Conversely, the shales of the upper Aeronian stage of the LMX Formation (SQ-11 and SQ-17), which belong to the shallow-water shelf facies, have the lowest mechanical values.

In general, the lower part of the Rhuddanian Stage of the LMX Formation and the Hirnantian and upper Katian stages of the WF Formation have higher values of E, H, and B. Table S4 indicates that the average values of micromechanical parameters (E, H, K_c, and B) in the WF Formation are relatively higher than those in the LMX Formation. The micromechanical parameters (E, H, K_c, and B) in the X1 plane are lower than those in the X3 plane.

删除[JianFeng Wang]: Table 2

删除[JianFeng Wang]: This leads to a significant enrichment of organic matter (possibly derived from siliceous organisms) in the WF shale.

删除[JianFeng Wang]: formation

删除[JianFeng Wang]: Table 2

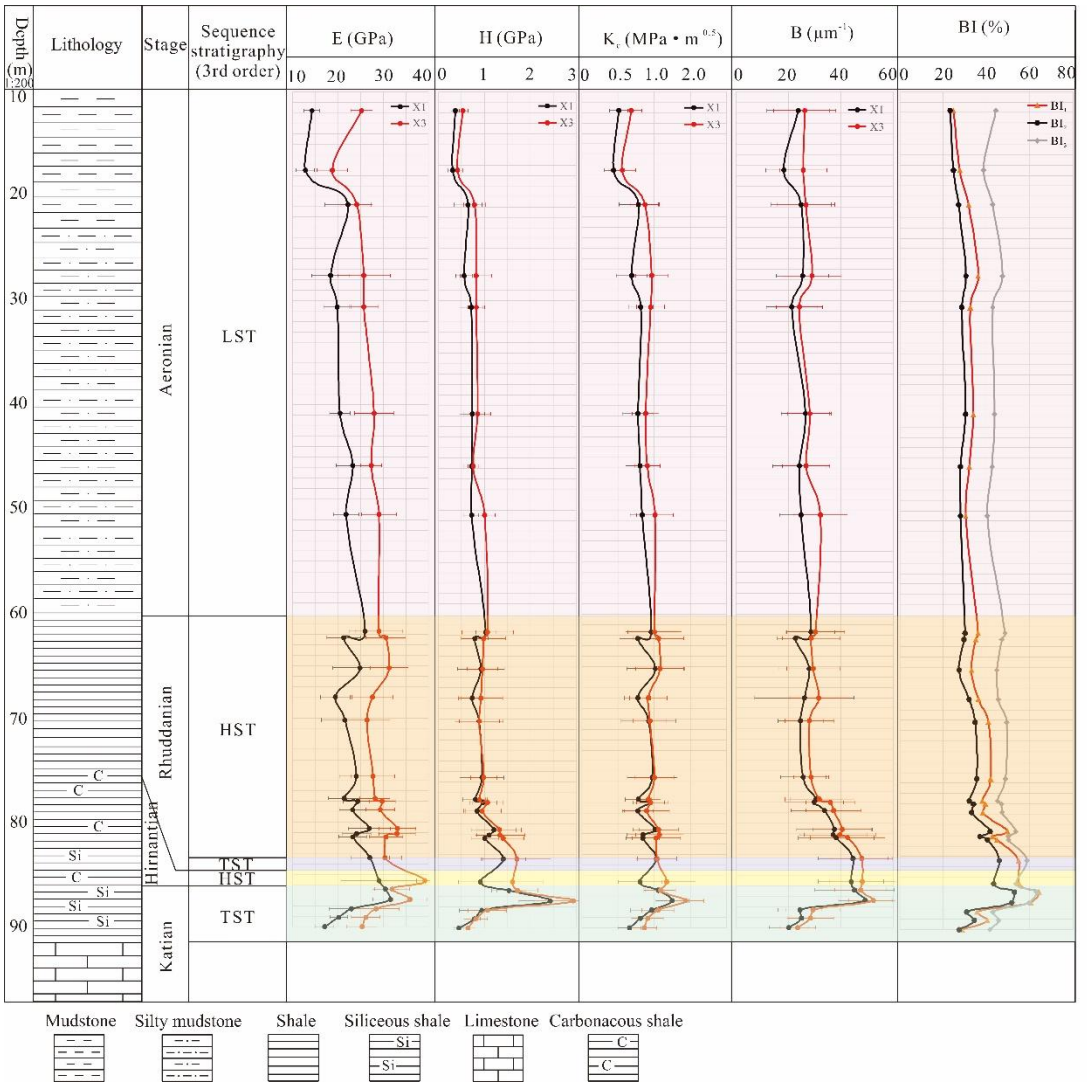

Figure 7. A histogram of E, H, K_c and BI (brittleness index) of shale in Well SQ-1. X1 indicates a direction perpendicular to the bedding plane of the shale, while X3 indicates a direction parallel to the bedding plane. BI_1, BI_2, and BI_3 are brittleness indices based on mineral composition (as shown in Table 4). From SQ-1 well bottom to the top, E, H, K_c, and BI all show the similar trend, and the bottom of LMX Formation and the upper part of WF Formation (~80-87 m) have large values.

5. Discussion

5.1 Paleo-depositional conditions of WF-LMX shales

删除[JianFeng Wang]:
Table 2. Composition and micromechanical parameters of shale samples
<sp>.
Note: The mineral content is the volume percentage, and the data are expressed as: the lowest value - the highest value (average value).

5.1.1 Sedimentary shale site

Al_2O_3 and TiO_2 are commonly used as indicators of terrigenous material, while Mn is considered a marker element from the deep ocean (Adachi et al., 1986, Boynton 1984). The MnO/TiO_2 ratio is generally less than 0.5 in coastal or continental shelf areas and ranges from 0.5 to 3.5 in open ocean or deep sea environments (Adachi et al., 1986, Boynton 1984, Sethi et al., 2024). The average MnO/TiO_2 value of 0.06 in the WF-LMX shales indicates a sedimentary environment closer to the continent. The $Al_2O_3/(Al_2O_3+Fe_2O_3)$ ratios in sediments from ridge, basin, and continental margin areas are less than 0.4, in the range of 0.4 to 0.7, and between 0.7 and 0.9, respectively (Murray et al., 1991). The $Al_2O_3/(Al_2O_3+Fe_2O_3)$ ratio of WF-LMX shales ranges from 0.65 to 0.78, with an average of 0.71, suggesting a continental margin sedimentary environment. In addition, the K_2O/Na_2O vs. SiO_2 and SiO_2/Al_2O_3 vs. K_2O/Na_2O plots can also be used to determine the ancient and modern tectonic backgrounds of the basins (Roser and Korsch 1988, Sethi et al., 2024). In Figure 8a-b, the WF-LMX shales show high SiO_2/Al_2O_3 ratios, K_2O/Na_2O ratios, and SiO_2 values. The majority of the data points are within the passive continental margin. Therefore, the WF-LMX shales in the study area are indicative of a passive continental margin sedimentary environment.

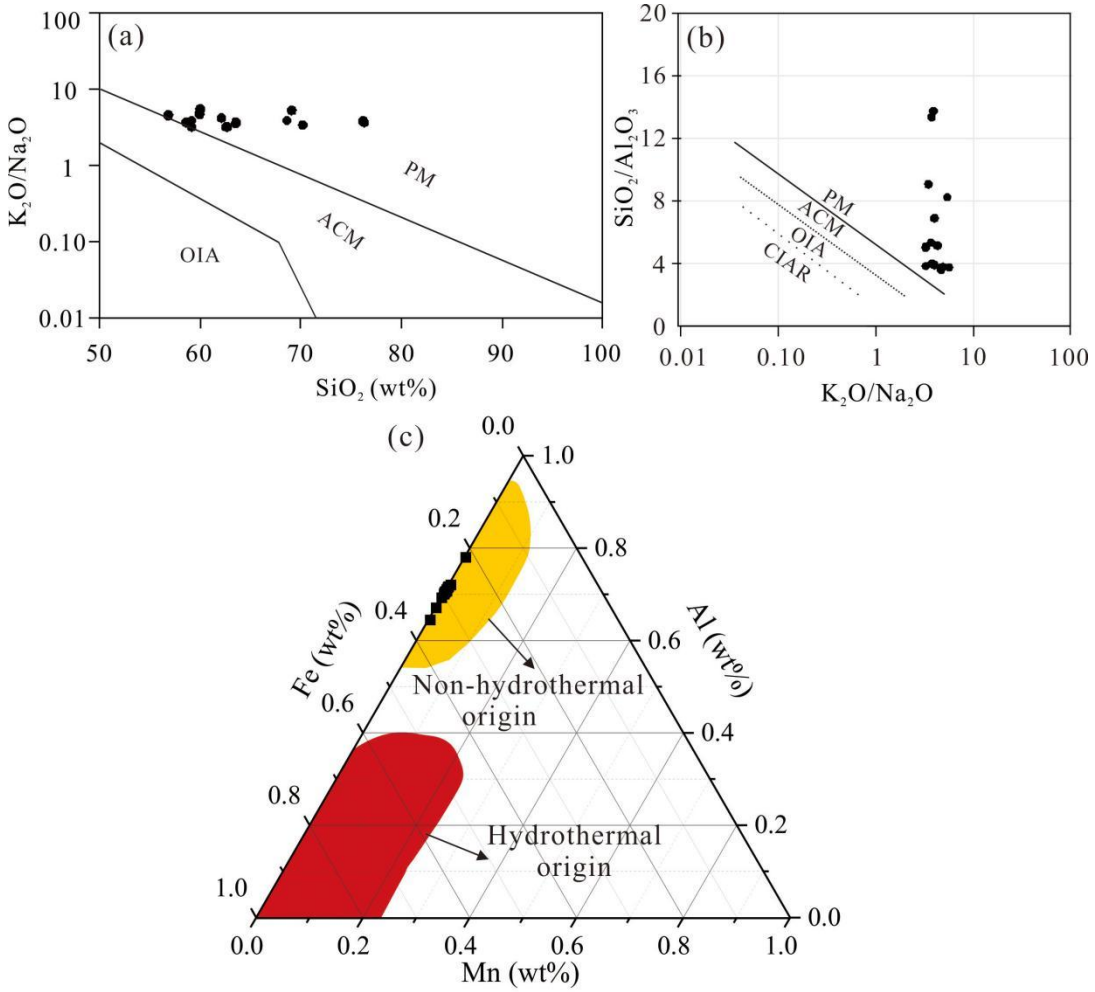

Figure 8. (a) Depositional position classification diagrams (a) (after Roser and Korsch. (1988)) and (b) (after Maynard. (1982)). Identification origin of hydrothermal-biogenic sedimentary (Adachi et al., 1986). PM=passive continental margin; ACM=active continental margin; CIAR=continental island arc; OIA=oceanic island arc.

5.1.2 Sources of silicon

Currently, the main sources of silicon in shales include biogenic, terrestrial detrital, and hydrothermal origins (Adachi et al., 1986, Reynolds and Verhoogen 1953). Al_2O_3 is typically indicative of terrestrial detrital input. When the SiO_2/Al_2O_3 ratio is close to 3, the silicon is primarily of crustal origin. However, when the ratio exceeds 3, silicon is primarily derived from

biogenic and hydrothermal processes (Boström et al., 1973). The SiO_2/Al_2O_3 values of the WF-LMX shales range from 3.63 to 13.73 (with an average of 6.42), suggesting that silicon in these shale samples is not primarily derived from terrestrial detrital sources. In particular, geochemical proxies such as (Fe + Mn)/Ti ratios above 25 ($\pm$5) and Al/(Al + Fe + Mn) ratios below 0.35 are recognized as the presence of hydrothermal activity during deposition (Boström and Peterson 1969, He et al., 2016). The WF-LMX shale samples exhibit (Fe + Mn)/Ti ratios ranging from 5.8 to 11.3, with an average of 8.9, while the Al/(Al + Fe + Mn) ratios exhibit a narrower range of 0.64 to 0.78, with an average of 0.71 across the data set. This result indicates that silicon in the WF-LMX shale samples is not primarily derived from hydrothermal sources. Furthermore, by observing the Mn-Al-Fe ternary diagram (Figure 8c), all the sample data fall within the non-hydrothermal origin range. It is commonly believed that a SiO_2/Al_2O_3 ratio exceeding 3.0 typically suggests a primarily biological origin (Boström et al., 1973). In the case of the WF-LMX shale samples, the SiO_2/Al_2O_3 values varied between 3.63 and 13.34, with an average of 6.42. This indicates that the silica source in these shale samples was predominantly influenced by biogenic input.

5.1.3 Paleoclimate and chemical weathering

Cox (1995) proposed the Index of Component Variation (ICV), which is calculated as the molar ratio of (Fe_2O_3+ K_2O + Na_2O + CaO* + MgO +MnO+TiO2), to Al_2O_3. According to Cullers et al. (2000), an ICV greater than 1 in fine-grained clastic rocks suggests low clay content and originally deposition in a tectonically active area. Conversely, an ICV less than 1 indicates high clay content resulting from chemical weathering or redeposition. In this study, the ICV values of

设置格式[JianFeng Wang]: 字体:（默认）Times New Roman, （中文）宋体

设置格式[JianFeng Wang]: 字体:（默认）Times New Roman, （中文）宋体

设置格式[JianFeng Wang]: 字体:（默认）Times New Roman, （中文）宋体

设置格式[JianFeng Wang]: 字体:（默认）Times New Roman, （中文）宋体

the samples (1.18-1.46, see Table S2) exceed 1, which confirms the first deposition without redeposition and can reflect the weathering degree and paleoclimate of the source area.

The process of chemical weathering typically results in the depletion of elements such as Ca, Na, and K, while promoting the relative accumulation of Al and Ti (Fedo et al., 1995, Nesbitt and Wilson 1992). To quantify the extent of chemical weathering in sediment source areas, previous researches have established indices such as the Chemical Index of Alteration (CIA = 100 × Al_2O_3 / (Al_2O_3 + CaO* + Na_2O + K_2O)) (Nesbitt and Wilson 1992, Nesbitt and Young 1982) and Plagioclase index of alteration (PIA) (PIA = 100 × (Al_2O_3 - K_2O) / ((Al_2O_3 - K_2O) + CaO* + Na_2O)) (Fedo et al., 1995). The units of the oxides used in these calculations are molar masses. CaO* refers specifically to the CaO content in silicate minerals. Since the CaO content in silicate minerals is often comparable to that of Na_2O, a correction method is applied: if the molar amount of CaO is greater than that of Na_2O, CaO = Na_2O; conversely, if the molar amount of CaO is less than that of Na_2O, no correction for CaO is required. The sample trend is generally parallel to the A-CN edge (Figure 9), indicating that potassium (K) has not been significantly leached during weathering and may be weakly affected by potassium metasomatism. In general, CIA values between 50-60 and PIA between 50-69 correspond to low weathering intensity, while CIA between 60-80 and PIA between 69-86 indicate moderate weathering, and CIA between 80-100 with PIA between 86-100 represent intense weathering conditions (Li et al., 2024, Nesbitt and Young 1982, Reimann and de Caritat 2012). For the WF-LMX shale samples, the calculated CIA indices range from 64.2 to 70.2 (mean = 65.9) (Figure 9; Table S2), and the PIA values range from 72.8 to 82.8 (mean = 76.94). These results indicate that the source rocks have experienced a consistent stable and moderate intensity of chemical weathering. In addition, the CIA index is

设置格式[JianFeng Wang]: 字体:（默认）Times New Roman, （中文）宋体

设置格式[JianFeng Wang]: 字体:（默认）Times New Roman, （中文）宋体

设置格式[JianFeng Wang]: 字体:（默认）Times New Roman, （中文）宋体

设置格式[JianFeng Wang]: 字体:（默认）Times New Roman, （中文）宋体

设置格式[JianFeng Wang]: 字体:（默认）Times New Roman, （中文）宋体

commonly used to evaluate paleoclimatic conditions (Fedo et al., 1995, Nesbitt and Wilson 1992). In hot, humid paleoclimates, CIA indexes fluctuate between 80 and 100, while warm, humid environments show values between 60 and 80. Conversely, cold, arid paleoclimates generally record CIA values in the range of 50 to 60 (Nesbitt and Wilson 1992). CIA values decrease from the lower to middle-upper part of the Wufeng Formation and then remain relatively stable at higher values in the Longmaxi Formation. This suggests that the paleoclimate shifted from warm and humid to cold and arid before returning to warm and humid conditions. However, the average CIA value of the WF-LMX Formation is 65.9, which generally indicates deposition under warm, humid conditions. It should be noted that this interpretation is based solely on major element data. To more precisely determine the paleoclimatic conditions, further validation through carbon-oxygen isotopes and palynological fossils is necessary.

设置格式[JianFeng Wang]: 字体:（默认）Times New Roman, （中文）宋体

设置格式[JianFeng Wang]: 字体:（默认）Times New Roman, （中文）宋体

删除[JianFeng Wang]: shale samples

设置格式[JianFeng Wang]: 字体:（默认）Times New Roman, （中文）宋体

删除[JianFeng Wang]: The average CIA value of WF-LMX shale samples is 65.9, indicating deposition in warm and humid paleoclimatic conditions.

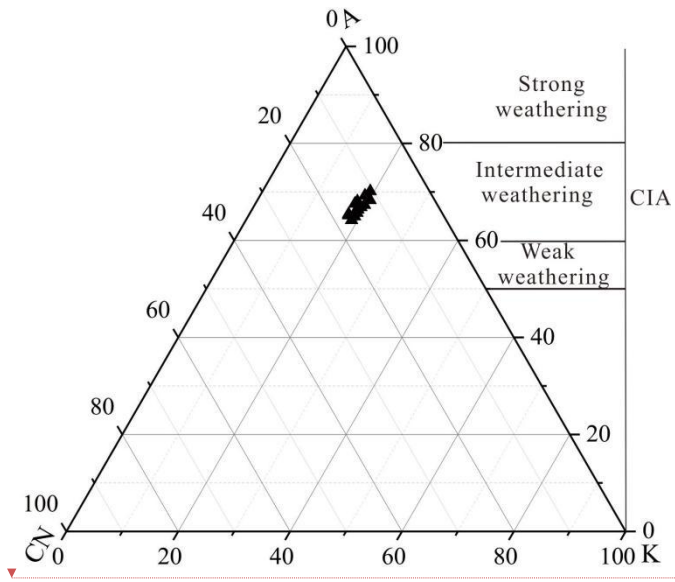

Figure 9. Temary plots of Al_2O_3 -(CaO* + Na_2O)-K_2O (A-CN-K) in molar proportions that reflecting the intensity of weathering (based map from (Nesbitt and Young 1982)). Here CaO* denotes the CaO content specifically within the silicate component.

513 **5.1.4 Redox conditions**

514 Previous studies have found that the redox indicators (e.g., U/Th, Ni/Co, and Mo values) of
515 the WF-LMX shales are positively correlated with TOC content (Li et al., 2017, Yan et al., 2018,
516 Wang et al., 2024, Wei et al., 2021). Based on the TOC content column profile of the SQ-1 well
517 (Figure6), it can be inferred that the bottom of the LMX Formation and the upper-middle part of
518 the WF Formation had the strongest reducing conditions, with TOC content exceeding 2.5%
519 formed in anoxic environments, while shale sections with TOC less than 2% were mainly formed
520 in oxic environments (Li et al., 2017). Furthermore, the high excess silicon content in organic-rich
521 shales in the middle-upper part of the WF Formation and the bottom of the LMX Formation
522 indicates relatively high paleoceanic productivity during deposition, which is consistent with
523 previous findings (Li et al., 2017, Yan et al., 2018).
524

525 **5.2 Effect of components on micromechanical properties**

526 **5.2.1 Young's modulus, hardness, and fracture toughness**

527 The sedimentary environment controls the mineral composition, TOC content, and pore
528 characteristics of organic-rich shales. Here we discuss the effect of constituents on the mechanical
529 properties of WF-LMX shales. For both X1 and X3 planes, the linear positive correlation between
530 Young's modulus of shale and the quartz content is good (Figure 10a). The reason is that quartz is
531 thought to be a brittle mineral. The measured Young's modulus of bulk shale is enhanced by
532 elevated concentrations of the quartz. In particular, Young's modulus of shale on both X1 and X3
533 planes and the content of excess SiO_2 show a positive correlation, especially for that on the X1
534 plane (Figure 10i). This means authigenic quartz plays an important role in increasing the strength

删除[JianFeng Wang]: **Paleosalinity and r**

删除[JianFeng Wang]: The MgO/Al_2O_3 ratio is used to quantify the extent of historical salinity in aquatic systems (Zhang 1988, Zhou et al., 2022). Specifically, MgO is indicative of aquatic origins, whereas Al_2O_3 is indicative of terrestrial environments. Consequently, this ratio serves as a proxy for paleosalinity within water bodies. A value less than 1 indicates a freshwater environment, a range of 1 to 10 indicates a brackish water environment, and a ratio greater than 10 indicates a saline environment (Zhang 1988). Analysis of the shale samples shows MgO/Al_2O_3 ratios ranging from 0.14 to 0.20 (mean = 0.17), indicating a freshwater depositional background.

设置格式[JianFeng Wang]: 字体:（默认）Times New Roman, （中文）宋体

设置格式[JianFeng Wang]: 字体:（默认）Times New Roman, （中文）宋体

of shale and improving the fracturability of the shale. Conversely, Young's modulus and clay mineral content show a negative correlation in different planes (Figure 10b).

As clay minerals inherently act as plastic components within shale matrices. While increased clay content decreases mechanical properties of shale, the scientific consensus remains unresolved regarding the brittle classification of feldspar, calcite, dolomite, and pyrite (Glorioso and Rattia 2012, Wang and Gale 2009).

As shown in Figures 10c-10f, the content of these minerals do not show a direct positive relationship with Young's modulus values. Notably, there is a negative correlation between calcite content and modulus measurements (Table 2, Figure 10c), which is consistent with previous triaxial compression studies of core samples (Diao 2013). This phenomenon may be due to two factors: (1) relatively low calcite volume fractions (vol.% < 8%), and (2) isolated grain distribution patterns within the shale matrix. Such dispersed rigid particles (calcite, dolomite, pyrite) fail to form effective load-bearing frameworks, thereby precluding embrittlement enhancement by mineral reinforcement.

删除[JianFeng Wang]: 3

Compared to inorganic minerals, organic matter has lower density (approximately half the density of the shale rock minerals), and much lower modulus values in the range of 1-20 GPa (Fender et al., 2020, Wang et al., 2024). However, Young's modulus is statistically positively correlated with TOC content of WF-LMX shales in both planes (Figure 10g). The reason is that the contents of quartz and organic matter show a synchronous and co-directional trend in the stratigraphic profile. While organic matter inherently reduces shale strength, quartz emerges as the primary determinant in increasing shale Young's modulus, thereby leading to a consistent contribution relationship between organic matter and the Young's modulus of shale. Young's

modulus shows no correlation with total nanopore volume or the total nanopore surface areas (Figure 10k-10l), and even a weak positive correlation with porosity (measured by MICP method) (Figure 10j). The main reason is that in the WF-LMX shale, high porosity and total pore volume are associated with high organic content (Table 2), which is positively correlated with the content of authigenic quartz. The influence of pores on shale mechanical properties may be compensated by authigenic quartz. On the other hand, the relationship between Young's modulus and individual components shows a more pronounced correlation in the X1 plane compared to the X3 plane, a disparity that could be primarily due to the preferential orientation of mineral particles during sedimentation and the distinct mechanical behaviors inherent to their depositional environments.

删除[JianFeng Wang]: 3

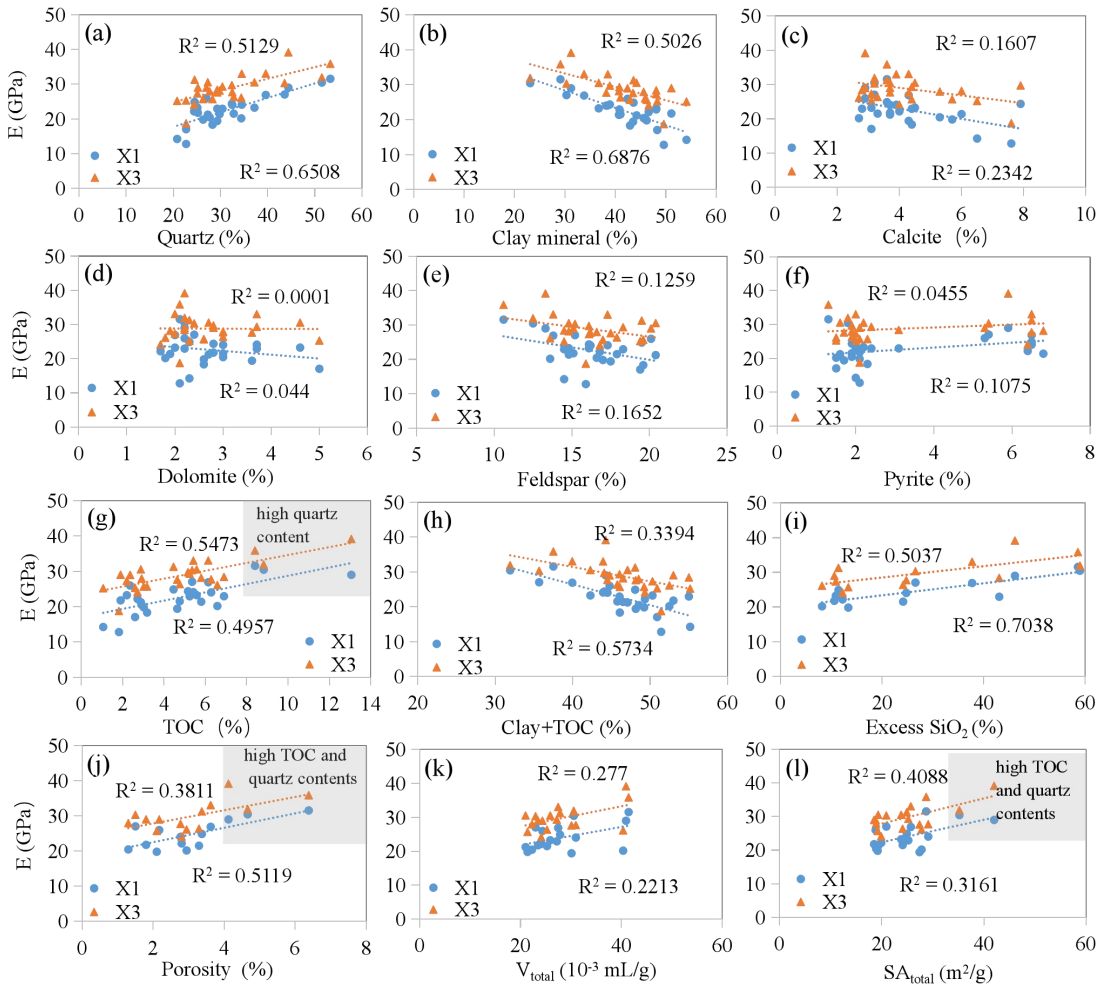

Figure 10. Correlation of shale Young's modulus (E) with volumetric proportions of matrix constituents (a-h), excess SiO_2 content (i), porosity (j), total nanopore volume (k), and surface areas (l). Note:Q=Quartz, F=Feldspar, Car=Carbonate, Dol=Dolmite, Py=Pyrite, V_{total}=the total nanopore volume, SA_{total}=the total nanopore surface areas. The percentage of various components is the volume percentage. The marked three samples in (g and j) are in high quartz, TOC contents and porosity. Young's modulus shows high dependence on quartz, clay, and clay +TOC content, especially along the X1 plane, while it has weak or no correlation with the change in the content of other rock constituents, including the carbonates, organics and pores.

Figure 11 shows a good positive linear relationship between Young's modulus and both hardness and fracture toughness. The relationship between Young's modulus and hardness exhibits greater strength along the X1 plane (R^2=0.74) compared to the X3 plane (R^2=0.60). Conversely, the correlation between Young's modulus and fracture toughness maintains comparable magnitudes in both the X1 and X3 planes (Figure 11). Generally, the influence of components on hardness or fracture toughness is equivalent to that of Young's modulus. This observation may be due to the fact that Young's modulus serves as a direct measure of material stiffness, with higher values corresponding to increased resistance to deformation and crack propagation, thereby contributing to higher fracture toughness values (Gupta et al., 2020).

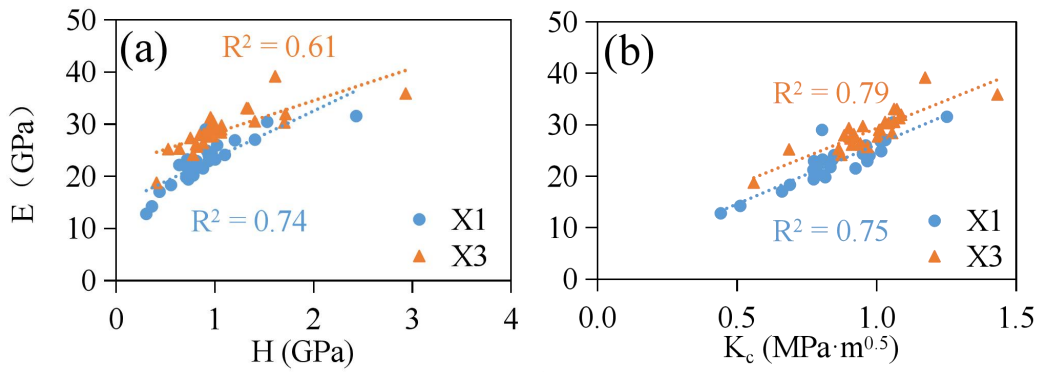

Figure 11. Relationships between E and (a) H, or (b) Kc.

Table 2 presents the statistical correlation analysis between the mechanical parameters and the mineralogical compositions, TOC content (volumetric fraction), porosity, and total pore volume for the shale samples via SPSS software. Similar to the linear fit results observed in Figure 10, the micromechanical properties (E, H, and K_c) of the WF-LMX shale show a good positive linear relationship with quartz, Q+Dol (quartz and dolomite), and QFC (quartz, feldspar, and carbonate) mineral assemblages, while exhibiting a negative correlation with clay mineral abundance and O/C (clay+TOC) composite content. Taken together, these relationships suggest that the micromechanical behavior of the shale is predominantly controlled by the proportional content of quartz, clay minerals, and organic-clay complexes, as these components form the primary structural framework of the shale matrix and collectively determine the overall mechanical performance of the WF-LMX Formation.

删除[JianFeng Wang]: 3

删除[JianFeng Wang]: formation

Table 2. Correlation matrix to investigate the dependence of mechanical parameters on mineralogy, TOC content (volume fraction), porosity and pore volume.

	TOC	Qtz	Clay	F	Cal	Dol	Py	O/C	Q+Dol	QFC	ϕ	PV_{total}	E1	E3	H1	H3	K_c1	K_c3	B1	B3
TOC	1.00																			
Qtz	0.82	1.00																		
Clay	-0.79	-0.93	1.00																	
F	-0.57	-0.66	0.43	1.00																
Cal	-0.32	-0.31	0.26	-0.02	1.00															
Dol	-0.12	-0.12	0.05	0.37	-0.02	1.00														
Py	0.24	0.05	-0.23	0.00	-0.13	-0.38	1.00													
O/C	-0.57	-0.85	0.95	0.31	0.19	0.01	-0.18	1.00												
Q+Dol	0.82	1.00	-0.93	-0.63	-0.32	-0.03	0.01	-0.85	1.00											
QFC	0.60	0.77	-0.88	-0.07	-0.22	0.25	-0.02	-0.88	0.80	1.00										
ϕ	0.72	0.56	-0.58	-0.40	-0.41	-0.39	0.16	-0.39	0.55	0.43	1.00									
PV_{total}	0.81	0.60	-0.43	-0.66	-0.43	-0.28	-0.03	-0.16	0.58	0.24	0.59	1.00								
E1	**0.70**	**0.81**	**-0.83**	-0.41	-0.48	-0.21	0.33	**-0.77**	**0.79**	**0.65**	0.50	0.47	1.00							
E3	**0.75**	**0.72**	**-0.71**	-0.36	-0.40	-0.01	0.21	-0.58	**0.72**	**0.62**	0.37	0.50	0.84	1.00						
H1	0.57	**0.86**	**-0.79**	-0.53	-0.33	-0.17	0.05	**-0.78**	**0.85**	**0.67**	0.40	0.45	0.85	0.69	1.00					
H3	**0.66**	**0.89**	**-0.80**	-0.57	-0.33	-0.09	0.03	**-0.75**	**0.89**	**0.69**	0.32	0.52	0.83	0.78	0.96	1.00				
K_c1	0.50	**0.69**	**-0.68**	-0.32	-0.46	-0.18	0.24	**-0.67**	**0.68**	0.57	0.55	0.32	0.89	0.65	0.88	0.77	1.00			
K_c3	**0.63**	**0.73**	**-0.68**	-0.31	-0.54	-0.06	0.14	**-0.60**	**0.72**	**0.62**	0.44	0.53	0.86	0.86	0.84	0.87	0.84	1.00		
B1	**0.75**	**0.91**	**-0.90**	-0.57	-0.26	-0.06	0.18	**-0.84**	**0.91**	**0.74**	0.42	0.47	**0.83**	**0.81**	**0.82**	**0.89**	**0.64**	**0.71**	1.00	
B3	**0.75**	**0.91**	**-0.88**	-0.59	-0.21	-0.03	0.10	**-0.81**	**0.92**	**0.74**	**0.62**	0.47	**0.80**	**0.80**	**0.81**	**0.89**	**0.60**	**0.70**	**0.98**	1.00

Note: Qtz = quartz, F = feldspar, Cal = calcite, Dol = dolomite, Py = pyrite O/C = clay + TOC, QFC = total volume content of quartz, feldspar, and carbonate minerals, ϕ = porosity, PV_{total} = total nanopore volume, Superscripts 1 and 3 after mechanical parameters denote measurements along the parallel bedding plane (X1) and perpendicular bedding plane (X3), respectively. $R^2 > 0.6$ are shown in bold. Negative signs (e.g. "-0.90") indicate inverse correlations between parameters. The micromechanical parameters (E, H, Kc, and B) show strong dependencies on quartz abundance, clay content, O/C ratio, Q+Dol assemblage, and QFC mineral fractions, with nearly all correlation coefficients exceeding 0.60. This underscores their dominant control over the mechanical behavior of the shale.

600

35

设置格式[JianFeng Wang]: 行距: 1.5 倍行距

删除[JianFeng Wang]:

删除[Jianfeng]: 3

5.2.2 Brittleness index

Table 2 shows that the B value based on micromechanical properties is strongly positively correlated with quartz (R^2=0.91), Q+Dol (R^2≥0.91) and QFC (R^2=0.74) contents, and negatively correlated with clay (R^2≥0.88), and clay+TOC contents (R^2≥0.81). However, no significant correlations were observed between these parameters and other individual minerals, porosity, or total nanopore volume. Notably, the R^2 values for the correlations between the brittleness index (B) and mineralogical constituents were similar to those for Young's modulus (E) and hardness (H), but had consistently higher magnitudes (Table 2). Therefore, quartz, especially for the authigenic quartz, as a distinct constituent of marine shale, plays an important role in enhancing the brittleness of shale. The B is strongly positively correlated with the E and H in both the planes, indirectly suggesting that the effect of component on B in shale is similar to that of E and H. To explain the accuracy of the brittleness index calculated based on micromechanical properties, mineral composition method and micromechanical properties based on nanoindentation method are compared to characterize the brittleness of shale. Due to the disunity of brittle minerals, three typical formulas based on mineral composition are each selected. Table 3 shows the brittle mineral and the corresponding formulas.

删除[JianFeng Wang]: 3

删除[JianFeng Wang]: 3

删除[JianFeng Wang]: 4

Table 3. Brittleness index model based on mineral composition (V=volume fraction).

删除[JianFeng Wang]: 4

Model	Equation	Brittle minerals	Reference
1	$BI_1=V_{Qtz}/(V_{Qtz}+V_{carb}+V_{clay})$	Quartz	Jarvie et al. (2007)
2	$BI_2=(V_{Qtz}+V_{Dol})/(V_{Qtz}+V_{carb}+V_{clay+TOC})$	Quartz and dolomite	Wang and Gale (2009)
3	$BI_3=(V_{Qtz}+V_{cab})/(V_{Qtz}+V_{carb}+V_{clay+TOC})$	Quartz and carbonate	Glorioso and Rattia (2012)

Figure 12 shows that the brittleness index has a better linear positive correlation with E along

the X1 plane than along the X3 plane. The correlations between BI_1 and E are the strongest among the brittleness indices (BI_1, BI_2, and BI_3) along both the X1 (R^2=0.70) and X3 planes (R^2=0.49). The correlation between the brittleness index (BI_1, BI_2, and BI_3) and H in the X1 plane is close to that in the X3 plane. The correlations between the brittleness index (BI_1, BI_2, and BI_3) and H are almost all larger than those between E and the brittleness indices. This suggests that H in the X3 plane is more sensitive to the brittleness index than E. The reason may be related to the presence of various mineral phases and their overall physical properties. E is an inherent property of a material, fundamentally related to atomic bonds, while H measures the resistance to local plastic deformation caused by mechanical indentation or wear, which mainly depends on the microstructure or the arrangement of molecules and atoms (Liu et al., 2021). This difference may lead to the varying correlations with the brittleness index. The B value, determined from the micromechanical properties calculated from nanoindentation, exhibits a strong correlation with the mineral component-based BI_1, BI_2, and BI_3 values (Figures 12g-i). Moreover, it shows a similar trend of changes, from the base to the top of the SQ-1 well, as the BI_1, BI_2, and BI_3 values, indicating a high brittleness index at the lower interval of the LMX Formation and the upper interval of the WF Formation, between ~80.0-87.0 m (Figure 7). Compared with Young's modulus from conventional logging, we can not only obtain the Young's modulus of shale via drill cuttings, but also predict its brittleness in the X1 and X3 planes (Figure 7). Therefore, nanoindentation technology shows great potential in predicting the brittleness index of shale.

删除[JianFeng Wang]: Compared with conventional logging data, we can predict the brittleness of shale in both X1 and X3 planes (Figure 7).

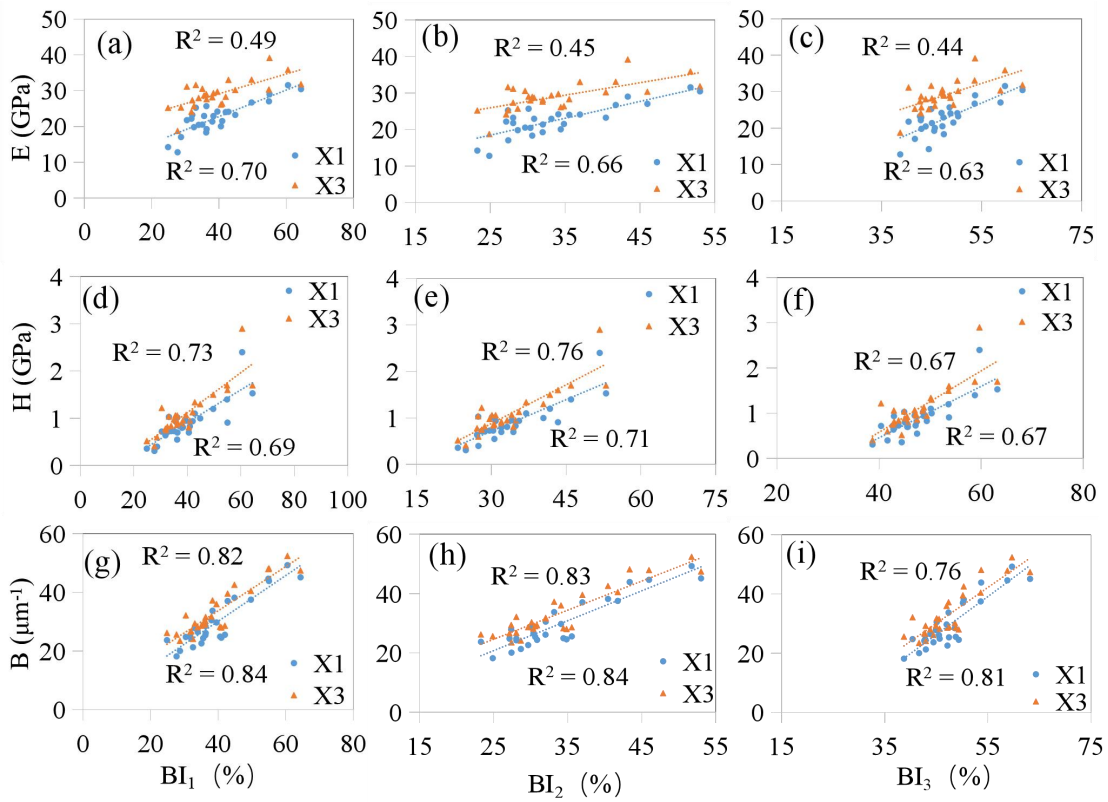

Figure 12. Relationship between Young's modulus (E), hardness, (H), brittleness index (B) based on the micromechanical properties and brittleness index (BI_1, BI_2, and BI_3) based on mineral composition of shale

5.3 Relationship between micromechanical properties and sedimentary environment

For all studied shale samples, they were all deposited in a passive continental margin environment, the depositional period was characterized by a warm and humid climate and a predominantly freshwater environment. Therefore, these factors are not the main reasons for the change in micromechanical properties of WF-LMX shales. However, changes in constituents (e.g., organic matter and biogenic silica), and redox conditions may have a significant effect on the variations in micromechanical properties of the shales. Previous studies have reported stratigraphic variations in mechanical properties of shales associated with different rock

mineralogy, which resulted from sea level cycles (Harris et al., 2011, Slatt and Abousleiman 2011), and were determined by the sedimentary environment. The WF Formation shales are located in a deep-water continental shelf sedimentary environment. They are located on a transgressive surface of erosion (TSE) or sequence boundary (SB) (Zheng et al., 2018). A decrease in clay minerals and an increase in organic matter and biogenic silica (excess SiO_2) were observed in the transgressive system tract (TST) of the WF Formation from the lower to the upper part, which is likely due to the change in relative sea level and sediment supply (Liu et al., 2019a). Young's modulus, hardness, and brittleness increase in the TST. The increase in diagenetic silica upward through the TST is also found in the Devonian gas shales of the Appalachian Basin, which increases the brittleness (Lash and Blood 2011). The Young's modulus, hardness and brittleness increase almost throughout the TST until reaching up to the maximum flooding surface (MFS), and then decrease slightly in the highstand systems tract (HST) (Figures 6 and 7).

The lower section of the LMX Formation primarily occupies a deep-water continental shelf, characterized by low-energy and strong reduction conditions, resulting in the deposition of mainly gray-black shale. During the later stages of sedimentation in the LMX Formation, the sea level dropped, and the sedimentary environment gradually shifted to oxidizing conditions and turbidite sediments, leading to the development of a lithological combination dominated by sandy mudstone and muddy siltstone (Figure 1). The LMX Formation locates on a relatively thin carbonaceous shale TST (at the bottom of Rhudianian stage), thicker lowstand systems tract (LST) and highstand systems tract (HST). In general, organic matter and biogenic silica (quartz) decrease sharply from the basal to the upper intervals of Rhudianian stage of the LMX Formation, while they decrease slightly in the LST of Aeronian stage in the LMX Formation. Similarly, there is a

decrease in Young's modulus, hardness and brittleness in the HST, followed by a slight decrease in the LST. The HST in the LMX Formation records a large decrease in biogenic silica and organic matter input, which contributes to the decrease in hardness and brittleness. In contrast, the LST records a small decrease in silica and an increased flux of terrigenous clay minerals, resulting in a lower hardness and brittleness (Figures 6 and 7). In general, the elevated values of Young's modulus, hardness and brittleness values are in the middle upper part of the TST in the Katian stage, the HST, the TST in the Hirnantian stage and the bottom part of the HST in the Rhudianian stage, which belong to the deep-water shelf facies, corresponding to a high content of biogenic silica and organic matter, which may be the optimal intervals for hydraulic stimulation in these areas.

6. Conclusions

In this paper, we applied nanoindentation mechanical testing along with rock mineralogical, major elemental, and pore analyses to quantitatively evaluate the mechanical profile of WF-LMX shales, and the relationship between micromechanical properties and the sedimentary conditions of marine shale Formation from the WF-LMX member in the shallow SQ-1 well, Sichuan Basin, Southwest China. The results were as follows:

(1) The WF-LMX shales within the study region were deposited in a passive margin environment. Biogenic silica was the major source.

(2) The micromechanical properties varied synchronously with mineral and organic content across the vertical drilling profile, reflecting changes in lithology and sedimentary condition within the WF-LMX Formations. Specifically, in the SQ-1 well, the micromechanical properties

删除[JianFeng Wang]: formation

删除[JianFeng Wang]: s

删除[JianFeng Wang]: The sedimentation period was characterized by warm and humid climatic conditions, predominantly in a freshwater environment.

of the shales in the WF-LMX Formation exhibit a distinct vertical pattern from bottom to top, sequentially passing through low, high and low intervals., which is relatively consistent with the variation of quartz and TOC content, whereas it is opposite to that of clay mineral content. We interpret these different trends as essentially dominated by the sedimentary environment of shale.

(3) Young's modulus shows a positive linear correlation with quartz content and TOC content, and a negative linear correlation with clay minerals, clay+TOC content. There are no or weak correlations with other individual minerals or porosity, suggesting that the micromechanical properties of LMX shale are primarily controlled by quartz content, clay minerals, and organoclay complexes. Autochthonous quartz contributes significantly to the elevated bulk Young's modulus values of the shale.

(4) The mineral content/Young's modulus relationship shows a stronger correlation in the X1 plane compared to the X3 plane, and the influence of components in shale on hardness or fracture toughness is equivalent to that of Young's modulus.

(5) The mineralogy-based brittleness index exhibits a good positive linear correlation with both Young's modulus and hardness, with a slightly better correlation observed for hardness. Besides, the brittleness index based on micromechanical properties shows a significant consistency with the index based on mineral composition. Based on the nanoindentation method, the lower section of the LMX Formation and upper section of the WF Formation, belonging to the deep-water shelf facies, have high brittleness index values, potentially making them ideal intervals for hydraulic stimulation in relevant areas.

Our observations here demonstrate the relationship between micromechanical properties and sedimentary environment of WF-LMX shale, and predict the optimal intervals for hydraulic

删除[JianFeng Wang]: formation

stimulation of WF-LMX shale by the brittleness index based on micromechanical properties. Future research can verify the effectiveness of micromechanics in predicting shale fracture intervals by actual field logging data, such as dynamic Young's modulus, thus expanding the application scope of micromechanics in this field.

Acknowledgements

This research was supported by the China Postdoctoral Science Foundation (2024M763277), the Postdoctoral Fellowship Program of CPSF (Grant No. GZC20241735), the National Natural Science Foundation of China (Grant No. 41802165 and Grant No. 42272182), the Basic and Applied Basic Research Project of Guangzhou City (Grant No. 2023A04J0208), and the Open Fund of Key Laboratory of Petroleum Resources Research, Gansu Province (SZDKFJJ2023009). The authors also thank Dr. Joanna Dziadkowiec and Prof. François Renard who for discussions.

Declaration of competing interest

The authors declare that they have no known competing financial interests or personal relationships that could have appeared to influence the work reported in this paper.

Data availability

The data that support the findings of this study are available from the corresponding author upon reasonable request.

Disclaimer

Publisher's note: Copernicus Publications remains neutral with regard to jurisdictional claims in published maps and institutional affiliations.

Author contributions

JW and CY were responsible for the design and methodology of the study, performed the experiments, assembled and analyzed the data, obtained and managed financial support, drafted and revised the paper. YL, WJ, YZ, and YL performed the experiments. YZ, QH, LF, YW, and YL collected the data. TZ, PP, and YX revised the draft. All authors contributed to the review of the article.

References

Abedi, S., Slim, M., and Ulm, F.-J.: Nanomechanics of organic-rich shales: the role of thermal maturity and organic matter content on texture. Acta Geotech., 11, 775-787. doi:10.1007/s11440-016-0476-2, 2016.

Adachi, M., Yamamoto, K., and Sugisaki, R.: Hydrothermal chert and associated siliceous rocks from the northern Pacific their geological significance as indication od ocean ridge activity. Sediment. Geol., 47, 125-148. doi:https://doi.org/10.1016/0037-0738(86)90075-8, 1986.

Alramahi, B., and Sundberg, M. I.: Proppant Embedment And Conductivity of Hydraulic Fractures In Shales. Paper presented at the 46th U.S. Rock Mechanics/Geomechanics Symposium, 2012.

Boström, K., Kraemer, T., and Gartner, S.: Provenance and accumulation rates of opaline silica, Al, Ti, Fe, Mn, Cu, Ni and Co in Pacific pelagic sediments. Chem. Geol., 11, 123-148. doi:https://doi.org/10.1016/0009-2541(73)90049-1, 1973.

Boström, K., and Peterson, M. N. A.: The origin of aluminum-poor ferromanganoan sediments in areas of high heat flow on the East Pacific Rise. Mar. Geol., 7, 427-447. doi:https://doi.org/10.1016/0025-3227(69)90016-4, 1969.

767 Boynton, W.: Cosmochemistry of the Rare Earth Elements: Meteorite Studies. In D. i.
768 Geochemistry (Ed.), 2, pp. 63-114. https://doi.org/10.1016/B978-0-444-42148-7.50008-3,
769 1984.
770 Charlton, T., Rouainia, M., Aplin, A., Fisher, Q., and Bowen, L.: Nanoindentation of Horn River
771 Basin Shales: The Micromechanical Contrast Between Overburden and Reservoir Formations.
772 J. Geophys. Res.: Solid Earth, 128, e2022JB025957. doi:10.1029/2022JB025957, 2023.
773 Chen, X., Fan, J., Chen, Q., Tang, L., and Hou, X.: Toward a stepwise Kwangsian Orogeny.
774 Science China Earth Sci. 57, 379-387. doi:10.1007/s11430-013-4815-y, 2014.
775 Cheng, Y. T., Li, Z., and Cheng, C. M.: Scaling relationships for indentation measurements. Philos.
776 Mag. A, 82, 1821-1829. 2002.
777 Cullers, R., and Podkovyrov, V.: Geochemistry of the Mesoproterozoic Lakhanda shales in
778 southeastern Yakutia, Russia: Implications for mineralogical and provenance control, and
779 recycling. Precambrian Res., 104, 77-93. doi:10.1016/S0301-9268(00)00090-5, 2000.
780 Curtis, M. E., Cardott, B. J., Sondergeld, C. H., and Rai, C. S.: Development of organic porosity in
781 the Woodford Shale with increasing thermal maturity. Int. J. Coal Geol., 103, 26-31.
782 doi:https://doi.org/10.1016/j.coal.2012.08.004, 2012.
783 Cox, R., Lowe, D., and Cullers, R.: The influence of sediment recycling and basement
784 composition on evolution of mudrock chemistry in the southwestern United States. Geochim.
785 Cosmochim. Acta, 59, 2919-2940. doi:10.1016/0016-7037(95)00185-9, 1995.
786 Diao, H.: Rock mechanical properties and brittleness evaluation of shale reservoir. Acta Petro. Sin.,
787 29, 3300-3306. 2013.
788 Du, J., Whittle, A. J., Hu, L., Divoux, T., and Meegoda, J. N.: Characterization of meso-scale
789 mechanical properties of Longmaxi shale using grid microindentation experiments. J. Rock
790 Mech. Geotech. Eng., 13, 555-567. doi:10.1016/j.jrmge.2020.09.009, 2021.
791 Fedo, C., Nesbitt, H., and Young, G.: Unraveling the effects of potassium metasomatism in
792 sedimentary rocks and paleosols, with implications for paleoweathering conditions and
793 provenance. Geology, 23, 921-924.
794 doi:10.1130/0091-7613(1995)023<0921:UTEOPM>2.3.CO;2, 1995.
795 Fender, T. D., Van Der Land, C., Rouainia, M., Graham, S. P., Jones, D. M., Vane, C. H., and
796 Wagner, T.: The Assessment of Organic Matter Young's Modulus Distribution With

删除[JianFeng Wang]:

删除[JianFeng Wang]:

删除[JianFeng Wang]:

797 Depositional Environment and Maturity. J. Geophys. Res.: Solid Earth, 125, e2020JB020435.
798 doi:10.1029/2020jb020435, 2020.
799 Gautham, S., and Sasmal, S.: Nano-scale fracture toughness of fly ash incorporated hydrating
800 cementitious composites using experimental nanoindentation technique. Theor. Appl. Fract.
801 Mech., 117, 103180. doi:https://doi.org/10.1016/j.tafmec.2021.103180, 2022.
802 Glorioso, J. C., and Rattia, A.: Unconventional reservoirs: basic petrophysical concepts for shale
803 gas. Paper presented at the SPE. 153004, pp. 1-38, 2012.
804 Guo, T., and Zeng, P.: The Structural and Preservation Conditions for Shale Gas Enrichment and
805 High Productivity in the Wufeng — Longmaxi Formation, Southeastern Sichuan Basin.
806 Energy Explor. Exploit., 33, 259-276. 2015.
807 Guo, T., Zhang, S., Qu, Z., Zhou, T., Xiao, Y., and Gao, J.: Experimental study of hydraulic
808 fracturing for shale by stimulated reservoir volume. Fuel, 128, 373-380.
809 doi:https://doi.org/10.1016/j.fuel.2014.03.029, 2014.
810 Guo, W., Shen, W., Li, X., Wang, N., Liu, X., Zhang, X., and Zhou, S.: Study on mechanical
811 characteristics and damage mechanism of the Longmaxi Formation shale in southern Sichuan
812 Basin, China. Energy Explor. Exploit., 38, 454-472. doi:10.1177/0144598719876858, 2019.
813 Gupta, I., Sondergeld, C., and Rai, C.: Applications of NanoIndentation for Reservoir
814 Characterization in Shales. In 52nd US Rock Mechanics/Geomechanics Symposium. 2018.
815 Gupta, I., Sondergeld, C., and Rai, C.: Fracture toughness in shales using nano-indentation. J.
816 Petro. Sci. Eng., 191, 107222. doi:10.1016/j.petrol.2020.107222, 2020.
817 Harris, N., Miskimins, J., and Mnich, C.: Mechanical anisotropy in the Woodford Shale, Permian
818 Basin: Origin, magnitude, and scale. The Leading Edge, 30, 284-291. doi:10.1190/1.3567259,
819 2011.
820 He, C., Ji, L., Wu, Y., Su, A., and Zhang, M.: Characteristics of hydrothermal sedimentation
821 process in the Yanchang Formation, south Ordos Basin, China: Evidence from element
822 geochemistry. Sediment. Geol., 345, 33-41. doi:https://doi.org/10.1016/j.sedgeo.2016.09.001,
823 2016.
824 Jarvie, D., Hill, R., Ruble, T., and Pollastro, R.: Unconventional shale-gas systems: The
825 Mississippian Barnett Shale of north-central Texas as one model for thermogenic shale-gas
826 assessment. AAPG bulletin, 91, 475-499. doi:10.1306/12190606068, 2007.

827 Jia, L., Xu, Q., and Zhang, L.: Assessment of deep shale fracture toughness using nanoindentation
828 tests. IOP Conf. Ser.: Earth Environ. Sci, 861, 062068. doi:10.1088/1755-1315/861/6/062068,
829 2021a.
830 Jia, Y., Tang, J., Lu, Y., and Lu, Z.: Laboratory geomechanical and petrophysical characterization
831 of Longmaxi shale properties in Lower Silurian Formation, China. Mar. Pet. Geol., 124,
832 104800. doi:https://doi.org/10.1016/j.marpetgeo.2020.104800, 2021b.
833 Kumar, V., Sondergeld, C. H., and Rai, C. S.: Nano to Macro Mechanical Characterization of
834 Shale. Paper presented at the In SPE annual technical conference and exhibition, SPE 159804.
835 https://doi.org/10.2118/159804-MS, 2012.
836 Larsson, P. L., Giannakopoulos, A. E., Sderlund, E., Rowcliffe, D. J., and Vestergaard, R.:
837 Analysis of Berkovich indentation. International Journal of Solids & Structures, 33, 221-248.
838 doi:10.1016/0020-7683(95)00033-7, 1996.
839 Lash, G., and Blood, R.: Sequence stratigraphy as expressed by shale source rock and reservoir
840 characteristics—Examples from the Devonian succession, Appalachian Basin. AAPG Search
841 and Discovery, 80168. 2011.
842 Laugier, M. T.: Palmqvist indentation toughness in WC-Co composites. J. Mater. Sci. Lett., 6,
843 897-900. doi:10.1007/BF01729862, 1987.
844 Lawn, B. R., and Marshall, D. B.: Hardness, Toughness, and Brittleness: An Indentation Analysis.
845 J. Am. Ceram. Soc., 62, 347-350. doi:https://doi.org/10.1111/j.1151-2916.1979.tb19075.x,
846 1979.
847 Li, C., Ostadhassan, M., Abarghani, A., Fogden, A., and Kong, L.: Multi-scale evaluation of
848 mechanical properties of the Bakken shale. J. Mater. Sci., 54, 2133-2151.
849 doi:10.1007/s10853-018-2946-4, 2018.
850 Li, H., Li, D., He, Q., Sun, Q., and Zhao, X.: Controlling mechanism of shale palaeoenvironment
851 on its tensile strength: A case study of Banjiuguan Formation in Micangshan Mountain. Fuel,
852 355, 129505. doi:https://doi.org/10.1016/j.fuel.2023.129505, 2024.
853 Li, Y., Zhang, T., Ellis, G. S., and Shao, D.: Depositional environment and organic matter
854 accumulation of Upper Ordovician – Lower Silurian marine shale in the Upper Yangtze
855 Platform, South China. Palaeogeogr. Palaeoecl., 466, 252-264.
856 doi:https://doi.org/10.1016/j.palaeo.2016.11.037, 2017.

857 Liu, B., Schieber, J., Mastalerz, M., and Teng, J.: Organic matter content and type variation in the
858 sequence stratigraphic context of the Upper Devonian New Albany Shale, Illinois Basin.
859 Sediment. Geol., 383, 101-120. doi:https://doi.org/10.1016/j.sedgeo.2019.02.004, 2019a.
860 Liu, K., Jin, Z., Zeng, L., Ostadhassan, M., and Xu, X.: Understanding the creep behavior of shale
861 via nano-DMA method. Energy Rep., 7, 7478-7487.
862 doi:https://doi.org/10.1016/j.egyr.2021.10.099, 2021.
863 Liu, K., Jin, Z., Zeng, L., Ozotta, O., Gentzis, T., and Ostadhassan, M.: Alteration in the
864 mechanical properties of the Bakken during exposure to supercritical CO2. Energy, 262,
865 125545. doi:https://doi.org/10.1016/j.energy.2022.125545, 2022.
866 Liu, K., Ostadhassan, M., and Bubach, B.: Applications of nano-indentation methods to estimate
867 nanoscale mechanical properties of shale reservoir rocks. J. Nat. Gas Sci. Eng., 35,
868 1310-1319. doi:10.1016/j.jngse.2016.09.068, 2016.
869 Liu, Y.: Fracture toughness assessment of shales by nanoindentation. MS Thesis. University of
870 Massachusetts Amherst. Cambridge, 2015.
871 Liu, Y., Xiong, Y., Liu, K., Yang, C., and Peng, P.: Indentation size and loading rate sensitivities on
872 mechanical properties and creep behavior of solid bitumen. Int. J. Coal Geol., 216, 103295.
873 doi:https://doi.org/10.1016/j.coal.2019.103295, 2019b.
874 Long, Y., Zhang, Y., Huang, X., Wang, Y., Zhao, Y., Wang, R., and Song, F.: Assessment of the
875 Multiphase Mechanical Properties of the Longmaxi Formation Shale Using Nanoindentation
876 Tests. ACS Omega, 6, 18200-18214. doi:10.1021/acsomega.1c02049, 2021.
877 Ma, Y., Zhong, N., Li, D., Pan, Z., Cheng, L., and Liu, K.: Organic matter/clay mineral
878 intergranular pores in the Lower Cambrian Lujiaping Shale in the north-eastern part of the
879 upper Yangtze area, China: A possible microscopic mechanism for gas preservation. Int. J.
880 Coal Geol., 137, 38-54. doi:https://doi.org/10.1016/j.coal.2014.11.001, 2015.
881 Manjunath, G. L., and Jha, B.: Geomechanical characterization of gondwana shale across
882 nano-micro-meso scales. Int. J. Rock Mech. Min. Sci., 119, 35-45.
883 doi:https://doi.org/10.1016/j.ijrmms.2019.04.003, 2019.
884 Maynard, J. B., Valloni, R., & Yu, H.S. Composition of modern deep-sea sands from arc-related
885 basins Geological Society of of London Special Publications, 10, 551–561. 1982.
886 Milliken, K. L., Ergene, S. M., and Ozkan, A.: Quartz types, authigenic and detrital, in the Upper

887 Cretaceous Eagle Ford Formation, South Texas, USA. Sediment. Geol., 339, 273-288.
888 doi:https://doi.org/10.1016/j.sedgeo.2016.03.012, 2016.
889 Murray, R. W., Buchholtz Ten Brink, M. R., Gerlach, D. C., Russ, G. P., and Jones, D. L.: Rare
890 earth, major, and trace elements in chert from the Franciscan Complex and Monterey Group,
891 California: Assessing REE sources to fine-grained marine sediments. Geochim. Cosmochim.
892 Acta, 55, 1875-1895. doi:https://doi.org/10.1016/0016-7037(91)90030-9, 1991.
893 Nesbitt, H., and Wilson, R.: Recent Chemical Weathering of Basalts. Am. J. Sci., 292, 740-777.
894 doi:10.2475/ajs.292.10.740, 1992.
895 Nesbitt, H. W., and Young, G. M.: Early Proterozoic climates and plate motions inferred from
896 major element chemistry of lutites. Nature, 299, 715-717. doi:10.1038/299715a0, 1982.
897 Oliver, W. C., and Pharr, G. M.: An improved technique for determining hardness and elastic
898 modulus using load and displacement sensing indentation experiments. J. Mater. Res., 7,
899 1564-1583. doi:10.1557/JMR.1992.1564, 1992.
900 Oliver, W. C., and Pharr, G. M.: Measurement of hardness and elastic modulus by instrumented
901 indentation: Advances in understanding and refinements to methodology. J. Mater. Res., 19,
902 3-20. 2004.
903 Reimann, C., and de Caritat, P.: New soil composition data for Europe and Australia:
904 Demonstrating comparability, identifying continental-scale processes and learning lessons for
905 global geochemical mapping. Sci. Total Environ., 416, 239-252.
906 doi:https://doi.org/10.1016/j.scitotenv.2011.11.019, 2012.
907 Reynolds, J. H., and Verhoogen, J.: Natural variations in the isotopic constitution of silicon.
908 Geochim. Cosmochim. Acta, 3, 224-234. doi:https://doi.org/10.1016/0016-7037(53)90041-6,
909 1953.
910 Rickman, R., Mullen, M., Petre, E., Grieser, B., and Kundert, D. (2008). A Practical Use of Shale
911 Petrophysics for Stimulation Design Optimization: All Shale Plays Are Not Clones of the
912 Barnett Shale. Paper presented at the SPE Annual Technical Conference and Exhibition.
913 https://doi.org/10.2118/115258-MS
914 Roser, B. P., and Korsch, R. J.: Provenance signatures of sandstone-mudstone suites determined
915 using discriminant function analysis of major-element data. Chem. Geol., 67, 119-139.
916 doi:https://doi.org/10.1016/0009-2541(88)90010-1, 1988.

Schieber, J., Krinsley, D., and Riciputi, L.: Diagenetic origin of quartz silt in mudstones and implications for silica cycling. Nature, 406, 981-985. doi:10.1038/35023143, 2000.

Sethi, C., Hazra, B., Ostadhassan, M., Motra, H. B., Dutta, A., Pandey, J. K., and Kumar, S.: Depositional environmental controls on mechanical stratigraphy of Barakar Shales in Rajmahal Basin, India. Int. J. Coal Geol., 285, 104477. doi:https://doi.org/10.1016/j.coal.2024.104477, 2024.

Shi, X., He, Z., Long, S., Peng, Y., Li, D., and Jiang, S.: Loading rate effect on the mechanical behavior of brittle longmaxi shale in nanoindentation. Int. J. Hydrogen Energy, 44, 6481-6490. doi:10.1016/j.ijhydene.2019.01.028, 2019a.

Shi, X., Jiang, S., Lu, S., He, Z., Li, D., Wang, Z., and Xiao, D.: Investigation of mechanical properties of bedded shale by nanoindentation tests: A case study on Lower Silurian Longmaxi Formation of Youyang area in southeast Chongqing, China. Pet. Explor. Dev., 46, 163-172. doi:10.1016/s1876-3804(19)30016-3, 2019b.

Shi, X., Jiang, S., Wang, Z., Bai, B., Xiao, D., and Tang, M.: Application of nanoindentation technology for characterizing the mechanical properties of shale before and after supercritical CO2 fluid treatment. J. CO2 Util., 37, 158-172. doi:10.1016/j.jcou.2019.11.022, 2020.

Shukla, P., Kumar, V., Curtis, M., Sondergeld, C. H., and Rai, C. S.: Nanoindentation Studies on Shales. Paper presented at the 47th U.S. Rock Mechanics/Geomechanics Symposium, San Francisco, California, 2013.

Slatt, R. M., and Abousleiman, Y.: Merging sequence stratigraphy and geomechanics for unconventional gas shales. The Leading Edge, 30, 274-282. doi:10.1190/1.3567258, 2011.

Sone, H., and Zoback, M. D.: Mechanical properties of shale-gas reservoir rocks — Part 1: Static and dynamic elastic properties and anisotropy. Geophysics, 78, D381-D392. doi:10.1190/geo2013-0050.1, 2013a.

Sone, H., and Zoback, M. D.: Mechanical properties of shale-gas reservoir rocks — Part 2: Ductile creep, brittle strength, and their relation to the elastic modulus. Geophysics, 78, D390-D399. 2013b.

Ulm, F.J., and Abousleiman, Y.: The nanogranular nature of shale. Acta Geotech., 1, 77-88. doi:10.1007/s11440-006-0009-5, 2006.

Ulm, F. J., Delafargue, A., and Constantinides, G.: Experimental Microporomechanics: Springer

Vienna, 2005.

Wang, F. P., and Gale, J. F.: Screening criteria for shale-gas systems. Gulf Coast Association of Geological Societies Transactions, 59, 779-793. 2009.

Wang, J., Dziadkowiec, J., Liu, Y., Jiang, W., Zheng, Y., Xiong, Y., Peng, P. a., and Renard, F.: Combining atomic force microscopy and nanoindentation helps characterizing in-situ mechanical properties of organic matter in shale. Int. J. Coal Geol., 281, 104406. doi:https://doi.org/10.1016/j.coal.2023.104406, 2024.

Wang, J., Yang, C., Liu, Y., and Xiong, Y.: Nanoindentation investigation of mechanical and creep properties of continental Triassic Yanchang Formation shale, Ordos Basin. Interpretation, 10, SJ29-SJ41. https://doi.org/10.1190/int-2021-0218.1, 2022a.

Wang, J., Yang, C., Liu, Y., Li, Y., and Xiong, Y.: Using Nanoindentation to Characterize the Mechanical and Creep Properties of Shale: Load and Loading Strain Rate Effects. ACS Omega, 7, 14317-14331. doi:10.1021/acsomega.2c01190, 2022b.

Wang, J., Liu, Y., Yang, C., Jiang, W., Li, Y., Xiong, Y., and Peng, P. a.: Evolution of mechanical properties of kerogen with thermal maturity. Mar. Pet. Geol., 145, 105906. doi:https://doi.org/10.1016/j.marpetgeo.2022.105906, 2022c.

Wang, J., Liu, Y., Yang, C., Zheng, Y., Jiang, W., Menegon, L., Renard, F., Peng, P. a., and Xiong, Y.: Upscaling the creep behavior of clay-rich and quartz-rich shales from nanoindentation measurements: Application to the Wufeng-Longmaxi shale, China. Int. J. Rock Mech. Min. Sci., 171, 105580. doi:https://doi.org/10.1016/j.ijrmms.2023.105580, 2023.

Wang, Q., Feng, Y., Gao, P., Meng, G., Lu, C., Fan, Q., Li, G., Tan, Y., and Xiao, X.: Influence of the sedimentary environment of the Wufeng-Longmaxi shale on organic matter accumulation in the Dingshan area, Sichuan Basin. Front. Earth Sci., 12, 1457377. doi:10.3389/feart.2024.1457377, 2024.

Wei, C., Dong, T., He, Z., He, S., He, Q., Yang, R., Guo, X., and Hou, Y.: Major, trace-elemental and sedimentological characterization of the upper Ordovician Wufeng-lower Silurian Longmaxi formations, Sichuan Basin, south China: Insights into the effect of relative sea-level fluctuations on organic matter accumulation in shales. Mar. Pet. Geol., 126, 104905. doi:10.1016/j.marpetgeo.2021.104905, 2021.

Yan, C., Jin, Z., Zhao, J., Du, W., and Liu, Q.: Influence of sedimentary environment on organic

删除[JianFeng Wang]:

删除[JianFeng Wang]: a

设置格式[JianFeng Wang]: 字体:（默认）Times New Roman, （中文）等线, 图案: 清除(白色)

删除[JianFeng Wang]:

设置格式[JianFeng Wang]: 字体:（默认）Times New Roman, （中文）等线, 图案: 清除(白色)

删除[JianFeng Wang]: Wang, J., Yang, C., Liu, Y., Li, Y., and Xiong, Y.: Using Nanoindentation to Characterize the Mechanical and Creep Properties of Shale: Load and Loading Strain Rate Effects. ACS Omega, 7, 14317-14331. doi:10.1021/acsomega.2c01190, 2022b.

977 matter enrichment in shale: A case study of the Wufeng and Longmaxi Formations of the
978 Sichuan Basin, China. Mar. Pet. Geol., 92, 880-894.
979 doi:https://doi.org/10.1016/j.marpetgeo.2018.01.024, 2018.
980 Yang, C., Xiong, Y., Wang, J., Li, Y., and Jiang, W.: Mechanical characterization of shale matrix
981 minerals using phase-positioned nanoindentation and nano-dynamic mechanical analysis. Int.
982 J. Coal Geol., 229, 103571. doi:10.1016/j.coal.2020.103571, 2020.
983 Yang, Z., Wang, L., Chen, Z., Xiang, D., Hou, D., Ho, C. L., and Zhang, G.: Micromechanical
984 Characterization of Fluid/Shale Interactions by Means of Nanoindentation. SPE Reservoir
985 Eval. Eng, 21, 405-417. doi:10.2118/181833-pa, 2018.
986 Yang, Z., Wang, L., Zhang, G., and Ho, C.: Micromechanical characterization of fluid-shale
987 interactions via nanoindentation. Paper presented at the SPE Asia Pacific Hydraulic
988 Fracturing Conference, 2016.
989 Zeng, Q., Feng, Y., and Xu, S.: A discussion of "Application of nano-indentation methods to
990 estimate nanoscale mechanical properties of shale reservoir rocks" by K Liu, M
991 Osatadhassan and B Bubach. J. Nat. Gas Sci. Eng., 42, 187-189.
992 doi:10.1016/j.jngse.2017.02.027, 2017.
993 Zeng, Q., Wu, Y., Liu, Y., and Zhang, G.: Determining the micro-fracture properties of Antrim gas
994 shale by an improved micro-indentation method. J. Nat. Gas Sci. Eng., 62, 224-235.
995 doi:10.1016/j.jngse.2018.12.013, 2019.
996 Zhao, J., Zhang, D., Wu, T., Tang, H., and Dai, C.: Multiscale Approach for Mechanical
997 Characterization of Organic-Rich Shale and Its Application. Int. J. Geomech., 19, 04018180.
998 2019.
999 Zhao, X., Li, Q., Jiang, Z., Zhang, R., and Li, H.: Organic geochemistry and reservoir
1000 characterization of the organic matter-rich calcilutite in the Shulu Sag, Bohai Bay Basin,
1001 North China. Mar. Pet. Geol., 51, 239-255.
1002 doi:https://doi.org/10.1016/j.marpetgeo.2013.12.014, 2014.
1003 Zheng, Y., Liao, Y., Wang, Y., Xiong, Y., and Peng, P. a.: Organic geochemical characteristics,
1004 mineralogy, petrophysical properties, and shale gas prospects of the Wufeng – Longmaxi
1005 shales in Sanquan Town of the Nanchuan District, Chongqing. AAPG Bull., 102, 2239-2265.
1006 doi:10.1306/04241817065, 2018.

删除[JianFeng Wang]: Zhang, S.: Study on the Ratio of Mg and Al in Sedimentary Layer and its Application. Bull. Mineralogy,Petrology Geochem.(in Chinese with English abstract), 1, 112-113. 1988.

Zheng, Y., Liao, Y., Wang, Y., Xiong, Y., and Peng, P. a.: The main geological factors controlling the Wufeng-Longmaxi shale gas content. AAPG Bull., 106, 2073-2102. doi:10.1306/07132218243 %J AAPG Bulletin, 2022.

Zou, C., Dong, D., Wang, S., Li, J., Li, X., Wang, Y., Li, D., and Cheng, K.: Geological characteristics and resource potential of shale gas in China. Pet. Explor. Dev., 37, 641-653. doi:10.1016/s1876-3804(11)60001-3, 2010.

删除[JianFeng Wang]: Zhou, T., Zhou, Y., Zhao, H., Li, M., and Mu, H.: Depositional Setting and Enrichment Mechanism of Organic Matter of Lower Cretaceous Shale in Ri-Qing-Wei Basin in the Central Sulu Orogenic Belt. Front. Earth Sci., 9, 808916. doi:10.3389/feart.2021.808916, 2022.